

**Effect of particle inertia on the alignment of small ice crystals in turbulent clouds**

K. GUSTAVSSON

*Department of Physics, Gothenburg University, 41296 Gothenburg, Sweden.*

M. Z. SHEIKH

*Univ. Lyon, ENS de Lyon, Univ. Claude Bernard, CNRS, Laboratoire de Physique, F-69342, Lyon, France.*

A. NASO

*Univ. Lyon, Ecole Centrale de Lyon, Univ. Claude Bernard, CNRS, INSA de Lyon, Laboratoire de Mécanique des Fluides et d'Acoustique, F-69134, Ecully, France.*

A. PUMIR

*Univ. Lyon, ENS de Lyon, Univ. Claude Bernard, CNRS, Laboratoire de Physique, F-69342, Lyon, France.*

B. MEHLIG

*Department of Physics, Gothenburg University, 41296 Gothenburg, Sweden.*

## ABSTRACT

Small non-spherical particles settling in a quiescent fluid tend to orient so that their broad side faces down, because this is a stable fixed point of their angular dynamics at small particle Reynolds number. Turbulence randomises the orientations to some extent, and this affects the reflection patterns of polarised light from turbulent clouds containing ice crystals. An overdamped theory predicts that turbulence-induced fluctuations of the orientation are very small when the settling number  $Sv$  (a dimensionless measure of the settling speed) is large. At small  $Sv$ , by contrast, the overdamped theory predicts that turbulence randomises the orientations. This overdamped theory neglects the effect of particle inertia. Therefore we consider here how particle inertia affects the orientation of small crystals settling in turbulent air. We find that it can significantly increase the orientation variance, even when the Stokes number  $St$  (a dimensionless measure of particle inertia) is quite small. We identify different asymptotic parameter regimes where the tilt-angle variance is proportional to different inverse powers of  $Sv$ . We estimate parameter values for ice crystals in turbulent clouds and show that they cover several of the identified regimes. The theory predicts how the degree of alignment depends on particle size, shape and turbulence intensity, and that the strong horizontal alignment of small crystals is only possible when the turbulent energy dissipation is weak, of the order of  $1\text{ cm}^2/\text{s}^3$  or less.

**1. Introduction**

As ice crystals settle through turbulent air, the turbulent velocity gradients tend to randomise their orientations. However, sometimes the crystals appear to align as they settle, so that they fall with a marked horizontal orientation. The effect can be observed in the form of light patterns above street lights during snow fall (Sassen 1980), ‘light pillars’, caused by specular reflection from the aligned ice-crystal platelets. The width of a light pillar is determined by the degree to which the crystal orientations are randomised.

The alignment of ice crystals in turbulent clouds has been systematically studied using LIDAR measurements (Sassen 1991; Noel and Chepfer 2004; Bréon and

Dubrule 2004). In cirrus clouds, the fluctuations of the crystal orientation with respect to the horizontal can be less than a few degrees (Sassen and Benson 2001; Noel and Chepfer 2004; Noel and Sassen 2005; Westbrook et al. 2010). Baran (2012) points out that aligned ice crystals affect the way in which clouds reflect radiation. High-altitude cirrus clouds tend to contain large ice mass. When such clouds cover a non-negligible part of the Earth’s atmosphere, ice-crystal alignment could affect its radiation balance, but the magnitude of this effect remains to be understood.

Hydrodynamic torques due to shape asymmetries or fluid-inertia can align the ice crystals. Rapidly settling particles experience a locally uniform flow-component (equal to the negative settling velocity). The resulting fluid-

inertia torque tends to orient small fore-aft symmetric and axisymmetric particles so that they fall with their broad sides down (Brenner 1961; Cox 1965; Khayat and Cox 1989; Dabade et al. 2015; Candelier and Mehlig 2016; Roy et al. 2019).

Turbulence, on the other hand, may upset the alignment. Early work concluded that turbulence has at most a minor effect on the alignment (Cho et al. 1981). The more recent analysis of Klett (1995) was carried out under the assumption that turbulent torques act as a white-noise signal on the settling particles. The resulting diffusion approximation simplifies the analysis, but it is justified at very high settling speeds only.

A systematic approach for small particles (Kramel 2017; Menon et al. 2017; Gustavsson et al. 2019; Anand et al. 2020) leads to the prediction of two very different regimes: at small settling speeds the orientation is random, while the particles are almost completely aligned at larger settling speeds. This theory assumes that the dynamics is overdamped, that particle inertia is negligible, in other words. In this extreme limit, the particles move in such a way that the instantaneous force and torque vanish, and the overdamped theory predicts a much stronger alignment at large settling speeds than the theory of Klett (1995). Is this difference due to the effect of particle inertia, neglected in the overdamped theory, but considered by Klett (1995)? After all, ice crystals are approximately 1000 times heavier than air, so particle inertia could have a significant effect upon their orientations.

To answer this question, we have investigated the effect of particle inertia upon the alignment of non-spherical particles settling through a turbulent flow, by analysing a statistical model of the effect. The main result of our analysis is that particle inertia may lead to significant fluctuations of the ‘tilt angle’ (Fig. 1). This effect results from a coupling between the fluctuations in the translational dynamics induced by turbulence, and the angular degrees of freedom. We find that the overdamped approximation applies only in a small region in the parameter plane. Even when particle inertia (measured by the ‘Stokes number’  $St$ ) is weak, it may nevertheless have a substantial effect on the particle orientation. This is the case when the settling speed is large (large ‘settling number’  $Sv$ ). Klett’s theory fails in this regime because it does not take into account translational particle inertia.

In short, the tilt-angle variance is much larger than previously thought. Particle inertia may increase typical tilt angles by several orders of magnitude compared with the overdamped limit, even at small  $St$ , and the theory predicts how typical tilt angles depend upon turbulence intensity, particle size, and shape. We validate the predictions of our new theory by numerical computations using statistical-model simulations and direct numerical simulations (DNS) of turbulence.

The general conclusion is diametrically opposite to that of Cho et al. (1981), who concluded that turbulence does not upset the alignment under realistic cloud conditions, in agreement with the prediction of the overdamped theory. Instead, properly taking into account particle inertia, we see that turbulence tends to misalign the orientations of the settling crystals, unless the turbulence level is very weak. This is consistent with the very strong alignment observed in cirrus clouds (Noel and Chepfer 2004; Noel and Sassen 2005), because these clouds have a very low turbulence intensity (Gultepe and Starr 1995).

Our theory for ice-crystal platelets may also explain why only a small fraction of ice crystals appears to align in more turbulent clouds (Bréon and Dubrulle 2004): the spatially varying conditions must be just right for strong alignment. A caveat, however, is that ice crystals come in a wide variety of shapes, symmetric but also asymmetric, even fractal, and sometimes hollow (Heymsfield 1973). The fraction of aligned ice crystals, and their average tilt-angle variance must depend on the distribution of shapes, sizes, and mass-density inhomogeneities.

The remainder of this paper is organised as follows. In Section 2 we give some background. Our model is summarised in Section 3, including a brief account of the overdamped theory (Kramel 2017; Menon et al. 2017; Gustavsson et al. 2019; Anand et al. 2020). Section 4 explains our method, an expansion in small tilt angles (Klett 1995). In Section 5 we describe the different physical regimes caused by particle inertia. Our theoretical results are summarised in Section 6 and discussed in Section 7, which also contains a detailed comparison with the theory of Klett (1995). Section 8 contains our conclusions. A complete summary of our calculations is given in a Supplemental Material.

## 2. Background

Ice crystals come in different shapes (Noel et al. 2006). Frequently observed shapes are columns (rod-like crystals) and platelets (disks) that exhibit discrete rotation symmetry with respect to a symmetry axis  $\hat{n}$ . Such platelets correspond to class P1a in the classification of Magono and Lee (1966). Commonly such crystals exhibit fore-aft symmetry. This means that particle shape is symmetric under  $\hat{n} \rightarrow -\hat{n}$ .

A small particle falling in a fluid experiences a mean flow corresponding to its negative settling velocity, plus fluctuations if the fluid is in motion (or is set into motion by the settling particle). Both mean flow and fluctuating fluid-velocity gradients give rise to torques that affect the orientation of a non-spherical particle. The relative importance of the two torques depends upon the settling speed, and on the shape of the particle.

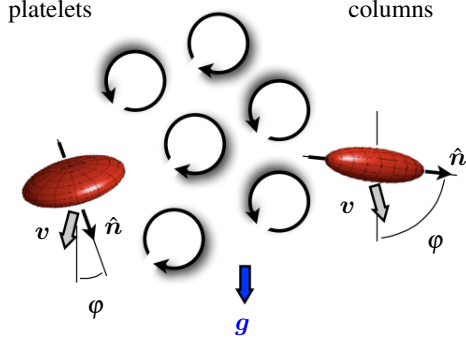


FIG. 1: Platelet (left) and column (right) settling in a turbulent flow. The particle symmetry axis is  $\hat{n}$ , and the particle velocity is denoted by  $v$ . Gravity  $\mathbf{g} = g\hat{\mathbf{g}}$  points downwards. The tilt angle is defined as  $\cos \varphi = \pm \hat{n} \cdot \hat{\mathbf{g}}$  (see text). In a quiescent fluid small columns fall with steady-state orientation  $\hat{n} \cdot \hat{\mathbf{g}} = 0$ , while platelets fall with steady-state orientation  $\hat{n} \cdot \hat{\mathbf{g}} = \pm 1$  (see text).

The mean flow causes a small axisymmetric particle with fore-aft symmetry and homogeneous mass distribution to align with respect to the direction of the gravitational acceleration  $\mathbf{g}$  (Brenner 1961; Cox 1965; Khayat and Cox 1989; Dabade et al. 2015; Candelier and Mehlig 2016), so that  $\hat{n} \perp \hat{\mathbf{g}}$  for columns, and  $\hat{n} \parallel \hat{\mathbf{g}}$  for platelets. The tilt angle is defined as  $\cos \varphi = \pm \hat{n} \cdot \hat{\mathbf{g}}$  (Fig. 1). We denote its deviations from the steady-state value by  $\delta\varphi$ , that is  $\varphi = \delta\varphi$  for platelets and  $\varphi = \frac{\pi}{2} + \delta\varphi$  for columns.

Several approaches have been proposed to study how turbulence affects the alignment of settling crystals. Motivated by the observation that crystal orientation determines the rate at which crystals are electrically charged, Cho et al. (1981) focused on the vorticity fluctuations in the fluid, neglecting the effect of the turbulent strain, and concluded that turbulence only weakly affects the crystal orientation. Klett (1995) formulated an elegant and more quantitative model describing the effect of turbulent vorticity and strain (Jeffery 1922) upon the orientation of settling crystals. The model determines how typical tilt angles depend on particle size and turbulent intensity. Klett's theory predicts that the tilt angle has a narrow distribution. For small particles, its variance decreases as

$$\langle \delta\varphi^2 \rangle \sim \frac{a^2}{\nu} \frac{\mathcal{E}}{W^2} \quad (1)$$

as the settling speed  $W$  increases. Here  $a$  is the particle size,  $\nu$  is the kinematic viscosity of air, and  $\mathcal{E}$  is the turbulent dissipation rate per unit mass. Klett's theory uses an approximate model for the inertial torque for nearly spherical particles (Cox 1965), valid at small particle Reynolds

number in steady flow. The theory is based on an expansion of the inertial angular dynamics in small  $\delta\varphi$ . Consistency with Eq. (1) requires that the settling speed is large so that  $\delta\varphi$  remains small. The theory also assumes that fluctuations in the settling speed due to translational particle inertia are negligible, and that the turbulent torques fluctuate very rapidly so that diffusion approximations can be used.

Gustavsson et al. (2019) computed the orientation variance in the opposite limit assuming that the angular dynamics is overdamped and that the turbulent fluid-velocity gradients experienced by the particle change slowly compared with the angular dynamics. In this persistent limit they found for spheroidal columns

$$\langle \delta\varphi^2 \rangle \sim C(\beta) \frac{\mathcal{E}\nu}{W^4}, \quad (2)$$

assuming that correlations between  $\hat{n}$  and the turbulent fluid velocities are negligible. The shape parameter  $C(\beta)$  in Eq. (2) is independent of the largest particle dimension,  $a$ , but it depends on particle shape through the particle aspect ratio  $\beta$ . For spherical particles  $\beta \rightarrow 1$ , and in this limit  $C(\beta)$  tends to zero. The slender-body limit corresponds to  $\beta \rightarrow \infty$ . In this limit Eq. (2) was derived by Kramel (2017) and Menon et al. (2017), yielding  $C(\beta) \sim \frac{32}{375} \log(\beta)^2$ . For platelets ( $\beta < 1$ ), the overdamped approximation works in the same way, resulting again in Eq. (2), but with a different prefactor (Anand et al. 2020).

At smaller settling speeds, the settling particles are approximately randomly oriented (Kramel 2017; Gustavsson et al. 2019). In this case, the distribution of  $n_g = \hat{n} \cdot \hat{\mathbf{g}}$  is uniform, so that one can compute the distribution of tilt angles via a change of variables. The resulting tilt-angle variance is of order unity:

$$\langle \delta\varphi^2 \rangle = O(1). \quad (3)$$

The transition between Eqs. (2) and (3) is quite sharp. Roughly speaking the overdamped theory says that the crystals are either randomly distributed or well aligned.

Kramel (2017) measured the orientation variance of nearly neutrally buoyant ramified particles in turbulence, triads made out of three slender rods. At larger settling speeds the experimental results are roughly consistent with Eq. (2), although the data lie somewhat below the theory. Kramel attributed this to the fact that the particles are larger than the Kolmogorov length and tend to average over small-scale turbulent fluctuations, reducing their effect. Lopez and Guazzelli (2017) measured the orientation distribution of slender columns settling in a two-dimensional steady vortex flow. They showed that the overdamped approximation describes the measured orientation distribution reasonably well. Both experiments were conducted in water with nearly neutrally buoyant particles,  $\rho_p/\rho_f \approx 1.15$  (Kramel 2017) and  $\rho_p/\rho_f \approx 1.038$  and 1.053 (Lopez and Guazzelli 2017).

Eq. (2) predicts a much faster decay of the orientation variance than (1) as the settling speed  $W$  increases. The question is how to reconcile the two estimates. For ice crystals in air the density ratio is large,  $\rho_p/\rho_f \approx 1000$ , so that the overdamped approximation leading to (2) may break down. Indeed, Eq. (2) predicts tilt-angle variances that are several orders of magnitude smaller than those observed in turbulent clouds (Bréon and Dubrulle 2004). Simulations of a statistical model for heavy non-spherical particles settling in turbulence indicate that particle inertia causes Eq. (2) to fail (Gustavsson et al. 2019). Klett’s theory takes into account rotational particle inertia, but it also fails to describe the simulation results of Gustavsson et al. (2019), possibly because the theory does not take into account translational particle inertia, which might affect the alignment indirectly since translation and rotation are coupled.

In summary, it is likely that rotational and translational particle inertia both have a substantial effect upon the orientation distribution of small crystals settling in a turbulent flow. Yet there is no theory for the effect of particle inertia that is consistent with known limits, and with results of statistical-model simulations. Earlier studies of particles settling in turbulence (Siewert et al. 2014a,b; Gustavsson et al. 2017; Jucha et al. 2018; Naso et al. 2018) included particle inertia, but disregarded the fluid-inertia torque.

### 3. Model

#### a. Turbulent fluctuations

Turbulent flows involve many eddies, covering a wide range of spatial and temporal scales. The smallest eddies are of the size of the ‘Kolmogorov length’  $\eta_K = (\frac{\nu^3}{\mathcal{E}})^{1/4}$ . The fastest time scale associated with the smallest eddies is the Kolmogorov time, defined as  $\tau_K = [2(\text{Tr}\mathbb{S}^2)]^{-1/2}$ , where  $\mathbb{S}$  is the strain-rate matrix, the symmetric part of the fluid-velocity gradient matrix. Equivalently, one can simply estimate the Kolmogorov time by  $\tau_K = (\frac{\nu}{\mathcal{E}})^{1/2}$ .

We use a statistical model (Gustavsson and Mehlig 2016) for the turbulent fluctuations. In this model, the fluid-velocity field is represented as an incompressible Gaussian random function with correlation length  $\ell$ , Eulerian correlation time  $\tau$  and Lagrangian correlation time  $\tau_K = \ell/(\sqrt{5}u_0)$  (‘Kolmogorov time’). Here  $u_0$  is the root mean square turbulent velocity. The model for the turbulent velocity and gradient correlations is described in the Supplemental Material, see Eq. (S25). The correlation length  $\ell$  is identified with the Taylor scale  $\lambda$  in turbulence. Since small eddies are swept by larger ones, fluid elements advected in turbulent flow decorrelate on the Lagrangian time scale,  $\tau_K$ , not on the Eulerian time scale. The statistical model has the same time scale,  $\tau_K$ , if the Kubo number,  $\text{Ku} = \tau/(\tau_K\sqrt{5})$  is large. In this limit, the statistical model is therefore expected to work well (Gustavsson and Mehlig 2016), provided that the particles are small enough, with

sizes in the dissipative range of turbulence, of the order of  $\ell$  and smaller. Otherwise inertial-range turbulent fluctuations might affect the particle dynamics, and such fluctuations are not taken into account in the statistical model.

Such fluctuations are contained in our model calculations based on DNS of turbulence, performed using the model for the particle dynamics described in Section 3.c. The simulations employ a fully dealiased pseudo-spectral code that solves the Navier-Stokes equation in a box with periodic boundary conditions, as described e.g. by Jucha et al. (2018). The size of the simulation domain was  $L \approx 6.3$  cm, the viscosity was  $\nu = 0.113$  cm<sup>2</sup>/s, and the turbulent dissipation rate  $\mathcal{E} \approx 1$  cm<sup>2</sup>s<sup>-3</sup>. Our simulations were run with a grid of size  $128^3$ . This means that they were well resolved, as can be judged by the value of  $k_{\text{max}}\eta_K \approx 3$ , where  $k_{\text{max}}$  is the largest wave number kept in the Fourier decomposition. The corresponding Taylor-scale Reynolds number is  $\text{Re}_\lambda \approx 56$ .

#### b. Parameters and dimensionless numbers

We consider particles with rotational symmetry and fore-aft symmetry. Commonly observed ice-crystal shapes (columns, platelets) fall into this class (Noel et al. 2006), although more complex shapes have been reported (Heymsfield et al. 2002a). The dimensions of the settling particle are characterised by the half-length of its symmetry axis,  $a_{\parallel}$ , and by the half-length of an orthogonal axis,  $a_{\perp}$ . The particle aspect ratio is defined as  $\beta = a_{\parallel}/a_{\perp}$ . In the following we consider prolate as well as oblate spheroids,  $\beta > 1$  (columns) and  $\beta < 1$  (platelets), because the hydrodynamic resistance tensors are exactly known for such particles. This simplification is quite common also in theories regarding other aspects of ice-crystal microphysics, such as crystal growth by vapor deposition (Chen and Lamb 1994), and provide a useful approximation to estimate the light reflection properties of crystals (Yang et al. 2013). We expect that the theory should work qualitatively for more general columnar and plate-like shapes (Fries et al. 2017). We define the largest particle dimension as

$$a = \max\{a_{\parallel}, a_{\perp}\}, \quad (4)$$

and assume that the particles have uniform mass density  $\rho_p$ . Note, however, that there are ice crystals in the atmosphere with non-uniform mass densities (Heymsfield et al. 2002b).

In addition to the Reynolds number  $\text{Re}_\lambda$  of the turbulent flow, the problem has at least six additional dimensionless parameters, summarised in Table 1. Particle shape is parameterized by its aspect ratio  $\beta$ . Particle size is parameterised by  $a/\eta_K$ . In the following we assume that this parameter is small, and we also assume that the particle is much heavier than the fluid

$$a/\eta_K \ll 1 \quad \text{and} \quad \rho_p/\rho_f \gg 1. \quad (5)$$

TABLE 1: Dimensionless parameters. The time scale  $\tau_p$  is the particle response time, Eq. (6). The Kolmogorov scales of the turbulence are denoted by  $\eta_K$  and  $\tau_K$ , and  $g$  is the magnitude of the gravitational acceleration.

$\beta = a_{\parallel}/a_{\perp}$	particle aspect ratio
$a/\eta_K$	particle size
$\rho_p/\rho_f$	particle-to-fluid density ratio
$St = \tau_p/\tau_K$	Stokes number (particle inertia)
$Sv = g\tau_p \tau_K/\eta_K$	settling number (settling speed)
$\ell/\eta_K$	turbulent correlation length

The Stokes number  $St = \tau_p/\tau_K$  is a dimensionless measure of particle inertia, where

$$\tau_p \equiv (2a_{\parallel}a_{\perp}\rho_p)/(9\nu\rho_f) \quad (6)$$

is an estimate of the particle-response time when  $\rho_p/\rho_f \gg 1$ . The settling number  $Sv = g\tau_p \tau_K/\eta_K$  is a dimensionless measure of the settling speed (Devenish et al. 2012). The last parameter is the turbulent correlation length,  $\ell/\eta_K$ .

### c. Equations of motion

Consider a small spheroidal particle settling through turbulent air, accelerated by the gravitational acceleration  $g$ . The particle is subject to a hydrodynamic force  $\mathbf{f}_h$  and to a hydrodynamic torque  $\boldsymbol{\tau}_h$ . Its translational motion is determined by Newton's second law:

$$\frac{d}{dt}\mathbf{x} = \mathbf{v}, \quad m\frac{d}{dt}\mathbf{v} = \mathbf{f}_h + m\mathbf{g}. \quad (7)$$

Here  $m$  is the particle mass,  $\mathbf{x}$  is the spatial position of the particle, and  $\mathbf{v}$  is its velocity. Particle orientation is defined by the unit vector  $\hat{\mathbf{n}}$  along the symmetry axis of the particle, and its angular velocity is denoted by  $\boldsymbol{\omega}$ . The angular equations of motion read:

$$\frac{d}{dt}\hat{\mathbf{n}} = \boldsymbol{\omega} \wedge \hat{\mathbf{n}}, \quad m\frac{d}{dt}[\mathbb{I}(\hat{\mathbf{n}})\boldsymbol{\omega}] = \boldsymbol{\tau}_h, \quad (8)$$

where  $\mathbb{I}(\hat{\mathbf{n}})$  is the rotational inertia tensor per unit mass in the lab frame (Supplemental Material).

A major difficulty lies in determining appropriate expressions for the hydrodynamic force and torque. Here we adopt a simplified model (Klett 1995; Kramel 2017; Lopez and Guazzelli 2017; Menon et al. 2017; Gustavsson et al. 2019), adding small inertial corrections due to convective fluid inertia to the standard expressions for  $\mathbf{f}_h$  and  $\boldsymbol{\tau}_h$  in the creeping-flow limit. In this limit the hydrodynamical force is just Stokes force:

$$\mathbf{f}_h^{(0)} = 6\pi a_{\perp}\mu\mathbb{A}(\hat{\mathbf{n}})(\mathbf{u} - \mathbf{v}), \quad (9)$$

where  $\mathbf{u} \equiv \mathbf{u}(\mathbf{x}, t)$  is fluid velocity at the particle position  $\mathbf{x}$ , and  $\mathbb{A}(\hat{\mathbf{n}})$  is a resistance tensor relating  $\mathbf{f}_h^{(0)}$  and the slip

velocity  $\mathbf{W} = \mathbf{v} - \mathbf{u}$  (Kim and Karrila 1991). Its elements depend on  $\beta$  and  $\hat{\mathbf{n}}$  (Supplemental Material). Since they are of order unity for platelets, Eq. (9) shows that Eq. (6) is a natural estimate of the particle response time for platelets of mass  $m \propto \rho_p a_{\parallel} a_{\perp}^2$ .

The hydrodynamic torque in the creeping-flow limit is (Jeffery 1922):

$$\boldsymbol{\tau}_h^{(0)} = 6\pi a_{\perp}\mu[\mathbb{C}(\boldsymbol{\Omega} - \boldsymbol{\omega}) + \mathbb{H}:\mathbb{S}]. \quad (10)$$

Here  $\boldsymbol{\omega} - \boldsymbol{\Omega}$  is the angular slip velocity, and  $\boldsymbol{\Omega} = \frac{1}{2}\nabla \wedge \mathbf{u}$  is half the fluid vorticity at the particle position. It is related to the asymmetric part  $\mathbb{O}$  of the matrix of fluid-velocity gradients by the relation  $\mathbb{O}\mathbf{r} = \boldsymbol{\Omega} \wedge \mathbf{r}$ . The symmetric part of the matrix of fluid-velocity gradients is denoted by  $\mathbb{S}$ , as mentioned above. The tensors  $\mathbb{C}(\hat{\mathbf{n}})$  and  $\mathbb{H}(\hat{\mathbf{n}})$  determine the coupling of the hydrodynamic torque to vorticity and strain (Kim and Karrila 1991). They depend on the instantaneous particle orientation  $\hat{\mathbf{n}}$  and on  $\beta$  (Supplemental Material).

Eqs. (9) and (10) neglect that the particle accelerates the surrounding fluid as it settles through the flow. For a particle falling through a fluid with a steady settling velocity, the slip velocity  $W$  generates fluid accelerations; it acts as a homogeneous background flow. To leading order in the particle Reynolds number

$$Re_p = aW/\nu \quad (a = \max\{a_{\parallel}, a_{\perp}\}), \quad (11)$$

the resulting steady convective-inertia corrections to the force and torque in a quiescent fluid are (Brenner 1961; Cox 1965; Khayat and Cox 1989; Dabade et al. 2015):

$$\mathbf{f}_h^{(1)} = -(6\pi a_{\perp}\mu)\frac{3}{16}\frac{aW}{\nu}[3\mathbb{A} - \mathbb{1}(\hat{\mathbf{W}} \cdot \mathbb{A}\hat{\mathbf{W}})]\mathbb{A}\mathbf{W}, \quad (12a)$$

$$\boldsymbol{\tau}_h^{(1)} = F(\beta)\mu\frac{a^3W^2}{\nu}(\hat{\mathbf{n}} \cdot \hat{\mathbf{W}})(\hat{\mathbf{n}} \wedge \hat{\mathbf{W}}). \quad (12b)$$

Here  $W = |\mathbf{W}|$  is the modulus of the slip velocity, and  $\hat{\mathbf{W}} = \mathbf{W}/W$  is its direction, and  $F(\beta)$  is a shape factor computed by Dabade et al. (2015). For slender columns, in the limit of  $\beta \rightarrow \infty$ , the shape factor tends to  $F(\beta) \sim -5\pi/[3(\log\beta)^2]$ . In this limit Eq. (12b) reduces to the slender-body limit derived by Khayat and Cox (1989). For nearly spherical particles the shape factor behaves as  $F(\beta) \sim \mp 811\pi\varepsilon/560$  for small eccentricity  $\varepsilon$ , defined by setting  $\beta = 1 + \varepsilon$  for prolate particles, and  $\beta = (1 - \varepsilon)^{-1}$  for oblate particles.

For a particle settling through a fluid, one must in principle consider the inertial effect due to gradients of the undisturbed fluid, parameterised by the shear Reynolds number  $Re_s = a^2s/\nu$ , where  $s$  is the shear rate (Subramanian and Koch 2005; Einarsson et al. 2015; Rosén et al. 2015). If we estimate typical turbulent shear rate by  $\tau_K^{-1}$ , we see that the model requires small particles, with particle sizes of the order of  $\eta_K$  or smaller (Candelier et al. 2016).

We also neglect possible effects of unsteady fluid inertia, a common approximation in the literature, and simply assume that force and torque on the settling particle are given by adding the steady inertial contributions (12) to Stokes force and Jeffery torque (Klett 1995; Kramel 2017; Lopez and Guazzelli 2017; Menon et al. 2017; Gustavsson et al. 2019). Lopez and Guazzelli (2017) demonstrated that this model can qualitatively describe the unsteady angular dynamics of rods settling in a vortex flow. The same model was used first by Klett (1995) to study the angular dynamics of nearly spherical particles settling in turbulence (we discuss the relation between Klett's and our own theory in Section 7.a). When the slip velocity varies rapidly, the steady model for the inertial torque may fail because the unsteady term in the Navier-Stokes equations may be equally or more important than the convective terms. We address this limitation of the model in our discussion, Section 7.d.

We non-dimensionalise Eqs. (7) to (12) with  $\tau_K$  and  $\eta_K$ :  $t' = t/\tau_K$ ,  $x' = x/\eta_K$ . To simplify the notation we drop the primes. The dimensionless equations of motion read:

$$\frac{d}{dt} \mathbf{x} = \mathbf{v}, \quad \text{St} \frac{d}{dt} \mathbf{v} = -\mathbb{A} \mathbf{W} + \text{Sv} \hat{\mathbf{g}}, \quad (13a)$$

$$\frac{d}{dt} \hat{\mathbf{n}} = \boldsymbol{\omega} \wedge \hat{\mathbf{n}}, \quad \text{St} \frac{d}{dt} \boldsymbol{\omega} = \text{St} \Lambda (\hat{\mathbf{n}} \cdot \boldsymbol{\omega}) (\boldsymbol{\omega} \wedge \hat{\mathbf{n}}) + \mathbb{I}^{-1} \mathbb{C} (\boldsymbol{\Omega} - \boldsymbol{\omega}) + \mathbb{I}^{-1} \mathbb{H} : \mathbb{S} + \mathcal{A}' (\hat{\mathbf{n}} \cdot \mathbf{W}) (\hat{\mathbf{n}} \wedge \mathbf{W}), \quad (13b)$$

with dimensionless parameters  $\text{St}$ ,  $\text{Sv}$ , and  $\beta$ . The tensors  $\mathbb{I}$ ,  $\mathbb{A}$ ,  $\mathbb{C}$ , and  $\mathbb{H}$  are given in the Supplemental Material. The shape factor  $\mathcal{A}'$  is defined as

$$\mathcal{A}' = \frac{5}{6\pi} F(\beta) \frac{\max(\beta, 1)^3}{\beta^2 + 1}, \quad (14)$$

and the parameter  $\Lambda = \frac{\beta^2 - 1}{\beta^2 + 1}$  was defined by Bretherton (1962). In Eq. (13) we neglected the inertial contribution (12a) to the hydrodynamic force, but kept the contribution (12b) to the hydrodynamics torque. In the theory and in the statistical-model simulations, the force corrections are not taken into account. Our numerical simulations with DNS of turbulence were performed both with and without the correction (12a).

#### d. Overdamped limit

Gustavsson et al. (2019) analysed the overdamped limit of a prolate spheroid settling in turbulence by taking the limit of  $\text{St} \rightarrow 0$  in Eq. (13), as suggested by Lopez and Guazzelli (2017). While Gustavsson et al. (2019) considered arbitrary aspect ratios for columns,  $\beta > 1$ , an equivalent approach was pursued by Kramel (2017) and by Menon et al. (2017) in the slender-body limit  $\beta \rightarrow \infty$ . In the overdamped limit  $\text{St} \rightarrow 0$ , the equations of motion (13)

take the form:

$$\mathbf{W} = \mathbf{W}^{(0)}(\hat{\mathbf{n}}) = \text{Sv} \mathbb{A}^{-1}(\hat{\mathbf{n}}) \hat{\mathbf{g}}, \quad (15a)$$

$$\boldsymbol{\omega} = \boldsymbol{\Omega} + \Lambda (\hat{\mathbf{n}} \wedge \mathbb{S} \hat{\mathbf{n}}) + \mathcal{A} \text{Sv}^2 (\hat{\mathbf{n}} \cdot \hat{\mathbf{g}}) (\hat{\mathbf{n}} \wedge \hat{\mathbf{g}}), \quad (15b)$$

$$\frac{d}{dt} \hat{\mathbf{n}} = \hat{\mathbf{n}} \wedge \boldsymbol{\omega}. \quad (15c)$$

Here  $\mathbf{W}^{(0)}(\hat{\mathbf{n}})$  is the steady slip velocity in the creeping-flow limit, of a spheroid subject to the gravitational acceleration  $\mathbf{g}$ . The shape factor  $\mathcal{A}$  is given by

$$\mathcal{A} = \mathcal{A}' I_{\perp} / (A_{\parallel} A_{\perp} C_{\perp}), \quad (15d)$$

where  $\mathcal{A}'$  was defined in Eq. (14). The remaining coefficients are elements of the particle-inertia tensor  $\mathbb{I}$  and the resistance tensors  $\mathbb{A}$  and  $\mathbb{C}$  (Supplemental Material).

Eq. (15b) illustrates how the fluid-velocity gradients compete with the torque due to convective fluid inertia. In the absence of flow, the angular dynamics is consistent with earlier results (Cox 1965; Khayat and Cox 1989; Dabade et al. 2015; Candelier and Mehlig 2016): for prolate particles it has a stable fixed point at  $\hat{\mathbf{n}} \cdot \hat{\mathbf{g}} = 0$ . This means that rods settle with their symmetry vector orthogonal to the direction of gravity,  $\hat{\mathbf{n}} \perp \hat{\mathbf{g}}$ , as mentioned above. For oblate particles there are two stable fixed points at  $\hat{\mathbf{n}} \cdot \hat{\mathbf{g}} = \pm 1$ , so that disks settle with their symmetry vector parallel with gravity,  $\hat{\mathbf{n}} \parallel \hat{\mathbf{g}}$ . In short, the effect of weak convective fluid inertia causes a small spheroid in a quiescent fluid to settle with its broad side first.

Turbulent velocity gradients modify the instantaneous fixed points of the angular dynamics, they change as the particle settles through the flow. The particle orientation  $\hat{\mathbf{n}}$  follows the fixed points quite closely if the fluid-velocity gradients change slowly compared to the stability time of the fixed point. This condition is satisfied for small  $\text{St}$  and large  $\text{Sv}$ . At first sight this may seem surprising because the fluid-velocity gradients vary very rapidly when  $\text{Sv}$  is large. But note that the stability time is even smaller, because of the  $\text{Sv}^2$ -factor in Eq. (15b)). In this limit the variance of the tilt angle  $\delta\varphi$  follows from the statistics of the fluid-velocity gradients. For columns Gustavsson et al. (2019) found:

$$\langle \delta\varphi^2 \rangle = \frac{\langle O_{12}^2 \rangle + \Lambda^2 \langle S_{12}^2 \rangle}{(\mathcal{A} \text{Sv}^2)^2} \propto \frac{\mathcal{E} \nu}{W^4}. \quad (16)$$

At large settling numbers one may neglect preferential sampling to obtain  $\langle O_{12}^2 \rangle = \frac{5}{3} \langle S_{12}^2 \rangle = \frac{1}{12}$  for isotropic homogeneous flows. Using  $W \sim \mathbf{W}^{(0)}(\hat{\mathbf{g}}) = \text{Sv}/A_{\perp}$  determines the shape parameter in Eq. (2), namely  $C(\beta) = \frac{5+3\Lambda^2}{60} \mathcal{A}^{-2} A_{\perp}^{-4}$  for columns. As  $\beta \rightarrow \infty$  we obtain  $C(\beta) \sim \frac{32}{375} \log(\beta)^2$ , so that Eq. (16) is consistent with the slender-body limit derived earlier by Kramel (2017). In homogeneous isotropic flows,  $C(\beta)$  is twice as large for platelets, compared with columns (Anand et al. 2020).

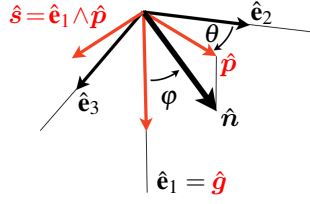


FIG. 2: Coordinate system for angular dynamics: direction of gravitational acceleration  $\hat{g} = \hat{e}_1$ , projection  $\hat{p}$  of  $\hat{n}$  onto the plane perpendicular to gravity, and  $\hat{s} = \hat{e}_1 \wedge \hat{p}$ .

#### 4. Small-angle expansion

When  $Sv$  is large, we expect the inertial torque to dominate the angular dynamics, leading to strong alignment of the settling crystals. In this limit the tilt-angle distribution is sharply peaked around  $\varphi^* = \frac{\pi}{2}$  for columns, and around  $\varphi^* = 0$  for platelets. In this case, it is sufficient to consider small deviations  $\delta\varphi = \varphi - \varphi^*$  from the steady-state angle, and to expand Eqs. (13) for  $|\delta\varphi| \ll 1$  as first suggested by Klett (1995). In the following we restrict the range of  $\varphi$  to  $0 \leq \varphi \leq \pi$  for columns, and to  $-\pi/2 \leq \varphi < \pi/2$  for platelets. Negative values of  $\varphi$  correspond to  $\hat{n} \cdot \hat{g} < 0$ .

A convenient coordinate system for the analysis is illustrated in Fig. 2. Namely, we take as coordinate axes gravity ( $\hat{g} = \mathbf{g}/|\mathbf{g}|$ ), the projection  $\hat{p}$  of  $\hat{n}$  onto the plane perpendicular to gravity (so that  $\hat{n} = \hat{g} \cos \varphi + \hat{p} \sin \varphi$  for  $\varphi > 0$ ), and  $\hat{s} = \hat{g} \wedge \hat{p}$ . In this coordinate system, the components of  $\hat{n}$  are  $n_g, n_p$ , and  $n_s = 0$ . We denote the corresponding components of other vectors and tensors using similar subscripts. We assume that the gravitational acceleration points in the  $\hat{e}_1$ -direction. The components of the particle-symmetry axis  $\hat{n}$  read

$$\hat{n} = \text{sgn}(\varphi) \begin{bmatrix} \cos \varphi \\ \sin \varphi \cos \theta \\ \sin \varphi \sin \theta \end{bmatrix}. \quad (17)$$

The orientation vector  $\hat{n}$  is determined by two angles, the tilt angle  $\varphi$ , and the angle  $\theta$  describing the orientation of the particle-symmetry vector  $\hat{n}$  in the plane orthogonal to gravity. The factor  $\text{sgn}(\varphi)$  is not strictly necessary, but it is convenient because it allows us to use Eq. (17) to parameterise  $\hat{n}$  for both columns and for platelets.

We project the angular dynamics (13b) onto the basis vectors  $\hat{g}$ ,  $\hat{p}$ , and  $\hat{s}$ , and expand to linear order in  $\delta\varphi$ . For platelets this gives:

$$\begin{aligned} \frac{d}{dt} \delta\varphi &= \omega_s, & \frac{d}{dt} \theta &= -\omega_p / \delta\varphi, \\ \frac{d}{dt} \omega_s &= \frac{C_{\perp}}{I_{\perp} St} (-\omega_s + Y_{gp} - Y_{gg} \delta\varphi) + \omega_p^2 / \delta\varphi, \\ \frac{d}{dt} \omega_p &= \frac{C_{\parallel}}{I_{\parallel} St} (-\omega_p - Y_{gs}) - \omega_p \omega_s / \delta\varphi, \\ \frac{d}{dt} \omega_g &= \frac{C_{\parallel}}{I_{\parallel} St} (-\omega_g + \Omega_g) + \frac{\delta\varphi}{St} \frac{C_{\perp}}{I_{\perp}} Y_{gs}. \end{aligned} \quad (18a)$$

TABLE 2: Time scales for Eq. (13) at large  $Sv$  (see text).

Time scale	parameter dependence
fluid-velocity gradients	$\tau_K = 1$
settling	$\tau_s = A^{(g)} \ell / Sv$
fluid-inertia torque	$\tau_{\varphi} = 1 / ( \mathcal{A}  Sv^2)$
damping	$\tau_d^{(tr)} = St / A^{(g)}$ (translation)
	$\tau_d^{(rot)} = I_{\perp} St / C_{\perp}$ (rotation)

For columns we obtain:

$$\begin{aligned} \frac{d}{dt} \delta\varphi &= \omega_s, & \frac{d}{dt} \theta &= \omega_g, \\ \frac{d}{dt} \omega_s &= \frac{C_{\perp}}{I_{\perp} St} (-\omega_s + Y_{gp} - Y_{gg} \delta\varphi), \\ \frac{d}{dt} \omega_p &= \frac{C_{\parallel}}{I_{\parallel} St} (-\omega_p + \Omega_p), \\ \frac{d}{dt} \omega_g &= \frac{C_{\perp}}{I_{\perp} St} (-\omega_g - Y_{sp} + \delta\varphi Y_{gs}). \end{aligned} \quad (18b)$$

In this small- $\delta\varphi$  expansion we neglected all terms of second and higher order in  $\delta\varphi$ . Amongst the terms linear in  $\delta\varphi$  we kept only those proportional to  $W_g$ , in keeping with our assumption that  $Sv$  is large. Amongst the terms quadratic in the angular velocity we kept only those terms that are multiplied by  $\delta\varphi^{-1}$ , the other quadratic terms are negligible unless  $St$  is large. Finally, we simplified the  $\theta$ -dynamics for platelets, Eq. (18a), neglecting a term proportional to  $\omega_g$  which is negligible compared to  $-\omega_p / \delta\varphi$  when  $\delta\varphi$  is small.

Eqs. (18) are driven by the matrix  $\mathbb{Y}$ , representing fluctuations of the fluid-velocity gradients ( $\mathbb{O}$  and  $\mathbb{S}$ ), and of the slip velocity  $\mathbf{W}$ . In the Cartesian basis, the elements of  $\mathbb{Y}$  read:

$$Y_{ij} = |\mathcal{A}| A^{(g)} A^{(p)} W_i W_j - O_{ij} - |\Lambda| S_{ij}. \quad (19)$$

We see that  $\mathbb{Y}$  represents two distinct origins of stochasticity. The first term on the r.h.s. of Eq. (19) stems from the fluctuations of the slip velocity  $\mathbf{W}$ . The two remaining terms model the effect of the turbulent fluid-velocity gradients, through the elements  $O_{ij}$  and  $S_{ij}$  of  $\mathbb{O}$  and  $\mathbb{S}$ .

#### 5. Analysis of time scales and physical regimes

Eq. (18) has four relevant time scales. First, the Kolmogorov time  $\tau_K$  (equal to unity in our dimensionless units) determines the magnitude of the fluid-velocity gradients. When the settling number  $Sv$  is small,  $\tau_K$  also determines the order of magnitude of the Lagrangian correlation time of tracer particles, of the same order as  $\tau_K$ , but usually somewhat larger.

Second, when  $Sv$  is large, the fluid velocity and the gradients seen by the settling particle decorrelate on the settling time scale  $\tau_s$ . Gustavsson et al. (2019) and Kramel (2017) estimated  $\tau_s$  as the time it takes to fall one flow-correlation length  $\ell$  with settling velocity Eq. (15a) in the

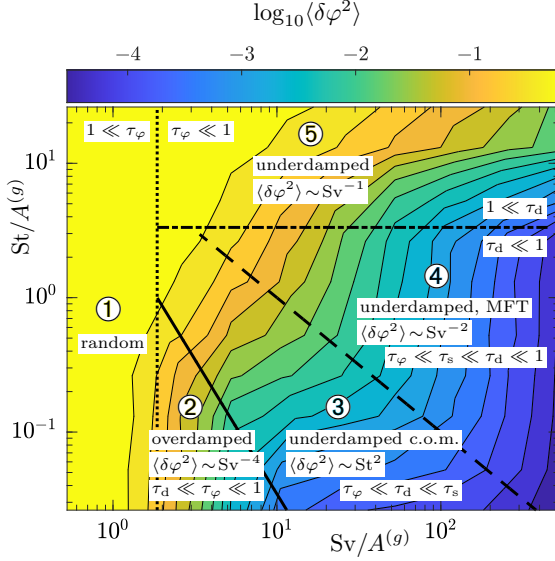


FIG. 3: Phase diagram of asymptotic regimes for the tilt-angle variance  $\langle \delta\varphi^2 \rangle$  in the statistical model, together with results of numerical statistical-model simulations of Eqs. (13) for platelets with  $\beta = 0.1$ ,  $\ell = 10$ , and  $Ku = 10$  (colour coded, see legend). The conditions separating the different regimes are discussed in the text:  $\tau_\varphi = 1$  (dotted line),  $\tau_\varphi = \tau_d^{(tr)}$  (solid line),  $\tau_d^{(tr)} = \tau_s$  (dashed line), and  $\tau_d^{(rot)} = 1$  (dash-dotted line). ‘MFT’ stands for mean-field theory (Section 5.d).

steady-state orientation in a quiescent fluid:

$$\tau_s = A^{(g)} \ell / Sv. \quad (20)$$

Third,  $\tau_\varphi$  describes the time scale of the fluid-inertia torque. In the overdamped limit the angular dynamics is determined by Eq. (15b). Because the fluid-velocity gradients are of order  $\sim \tau_K^{-1} = 1$ , the fluid-inertia torque dominates when  $|\mathcal{A}|Sv^2 \gg 1$ . Gustavsson et al. (2019) used

$$\tau_\varphi \equiv 1/(|\mathcal{A}|Sv^2), \quad (21)$$

the time it takes the overdamped angular dynamics to approach its steady state in a frozen flow. We expect that this remains a reasonable estimate of  $\tau_\varphi$  even outside the overdamped limit, provided that  $St$  is not too large. This time scale is related to  $\tau_{sed}$  considered by Kramel (2017), averaged over orientations.

Finally, the damping time scale describes the time scale of inertial effects in Eq. (18). In dimensionless units this time scale equals  $St$ , up to a prefactor determined by the shape coefficients in Eq. (18):

$$\tau_d = \begin{cases} St/A^{(g)} & \text{translation,} \\ I_\perp St/C_\perp & \text{rotation.} \end{cases} \quad (22)$$

As long as  $\beta$  is not too large, the coefficients  $A^{(g)}$  and  $C_\perp/I_\perp$  are of the same order for spheroids, so that  $\tau_d^{(tr)}$  and  $\tau_d^{(rot)}$  are of the same order. Where the quantitative difference matters we distinguish these time scales, otherwise we just write  $\tau_d$ . We remark that even though  $\tau_d^{(tr)}$  and  $\tau_d^{(rot)}$  are of the same order, they may in certain cases affect the rotational and translational dynamics differently. This is discussed below.

The dependence of these time scales upon the dimensionless parameters  $Sv$ ,  $St$ ,  $\beta$ , and  $\ell$  is summarised in Table 2. Comparing the time scales, we identify a number of asymptotic regimes of the angular dynamics (18) with qualitatively different physical behaviours. The different regimes are summarised in Fig. 3. The Figure also shows the tilt-angle variance obtained from numerical statistical-model simulations of Eqs. (13) (colour-coded contour plot), as well as the asymptotic statistical-model predictions derived in the following Sections. We see that the variance ranges over four orders of magnitude for the parameter ranges considered, and that there are five different asymptotic regimes with different mechanisms at work, leading to distinct scaling predictions for the variance.

#### a. Random orientation (regime ①)

When  $Sv$  is small so that  $\tau_\varphi \gg 1$ , the crystals are essentially randomly oriented as described in Section 2. In this regime the particle orientations are randomised by the turbulent fluid-velocity gradients. The symmetry-breaking torque due to settling does not matter, so that the tilt angles are randomly distributed with  $\langle \delta\varphi^2 \rangle \sim O(1)$ , Eq. (3).

#### b. Overdamped dynamics (regime ②)

When  $\tau_\varphi \ll 1$  and in addition  $\tau_d \ll \min\{\tau_\varphi, \tau_s\}$  then both angular and translational dynamics are overdamped. The persistent limit analysed by Gustavsson et al. (2019) corresponds to  $\tau_\varphi \ll \tau_s$  ( $\tau_s \ll \tau_\varphi$  can only occur for nearly spherical particles, see Section 7.a). When  $\tau_\varphi$  is much smaller than  $\tau_s$ , the fluid-velocity gradients remain constant during the time it takes for the tilt angle to adjust to its fixed point. The tilt-angle variance is determined by a balance between the turbulent fluid-velocity gradients and the inertial torque, and the variance is given by Eq. (16) for columns.

#### c. Underdamped centre-of-mass dynamics (regime ③)

The asymptotic regime ③ is delineated by the inequalities  $\tau_\varphi \ll \tau_d \ll \tau_s$  and  $\tau_d \ll 1$ . Since  $\tau_s \ll \min(1, \tau_s)$ , the angular dynamics is overdamped. But since  $\tau_d \gg \tau_\varphi$ , the overdamped approximation (15a) for the slip velocity does not apply, because the centre-of-mass (c.o.m.) dynamics does not have time to adjust to the rapid changes

in  $\delta\varphi$ . In this regime the tilt-angle variance is determined by the fluctuations of the underdamped c.o.m. dynamics, and therefore the variance depends only weakly on Sv, but strongly on St. The Jeffery torque (10) plays no role in this regime.

*d. Underdamped angular and c.o.m. dynamics, mean-field theory (regime ④)*

Passing from regime ③ to ④ in Fig. 3,  $\tau_d$  becomes larger than  $\tau_s$ . As a consequence, both c.o.m. and angular dynamics are underdamped. In this case the fluid velocity seen by the particle fluctuates more rapidly than the damping time scale. Within a mean-field theory (MFT), see Section II.C in the Supplemental Material, we find that the tilt-angle variance decays as  $\text{Sv}^{-2}$ , just like Eq. (1). But the prefactor is different from Klett's prediction (the Jeffery torque (10) does not matter in this regime).

*e. Underdamped angular and c.o.m. dynamics (regime ⑤)*

Regime ⑤ in Fig. 3 corresponds to  $\tau_\varphi \gg 1$  and  $\tau_d \gg 1$ . So the fluid-inertia torque dominates in this regime, and both c.o.m. and angular dynamics are underdamped. When in addition  $\tau_d \gg \tau_s$ , then the variance of the tilt angle decays as  $\text{Sv}^{-1}$ . We note that this asymptote is only reached for the largest St in Fig. 3. The opposite case,  $\tau_d \ll \tau_s$ , is very difficult to realise when  $\tau_d \gg 1$  and  $\tau_\varphi \gg 1$ .

In summary, the asymptotic regimes in Fig. 3 exhibit different power-law dependencies of the tilt-angle variance upon the settling number Sv. The different power-law scalings are visible as evenly spaced vertical or horizontal level curves in Fig. 3 (see also Fig. S1 in the Supplemental Material which shows the power laws more clearly). Since  $\text{Sv} \propto \tau_p \propto a^2$ , these statistical-model predictions translate into different power laws as a function of particle size. The overdamped regime ② has the strongest dependence on particle size,  $\langle \delta\varphi^2 \rangle \propto a^{-8}$ . However, Fig. 3 shows that regime ② is quite narrow, and in regimes ③ and ④ the variance decays more slowly with increasing particle size. The same conclusion holds for the transition from ① to ⑤.

## 6. Results

To determine the tilt-angle variance in regimes ③, ④, and ⑤, we solved the angular dynamics (18) together with that of  $Y_{ij}$  [Eq. (19)]. A brief yet complete account of our calculations is given in the Supplemental Material. The

result is:

$$\begin{aligned} \langle \delta\varphi^2 \rangle = f_\Lambda \left\{ \frac{A^{(g)2}}{\text{Sv}^2} C_u(0) + \frac{A^{(g)2}}{A^{(p)2} |\mathcal{A}|^2 \text{Sv}^4} C_B(0) \right. & (23) \\ + \frac{A^{(g)}}{|\mathcal{A}|^2 \text{StSv}^4} \int_0^\infty dt e^{-A^{(g)}t/\text{St}} \left[ \left( 1 - \frac{A^{(g)2}}{A^{(p)2}} \right) C_B(t) \right. & \\ \left. \left. + 2A^{(g)} |\mathcal{A}| \text{Sv} C_X(t) - A^{(g)2} |\mathcal{A}|^2 \text{Sv}^2 C_u(t) \right] \right\}. & \end{aligned}$$

Here  $f_\Lambda = 2$  for  $\Lambda < 0$  (platelets) and  $f_\Lambda = 1$  for  $\Lambda > 0$  (columns). Eq. (23) is expressed in terms of correlation functions of fluid velocities and fluid-velocity gradients evaluated along settling trajectories,  $C_B(t) = \langle O_{12}(t)O_{12}(0) + 2|\Lambda|O_{12}(t)S_{12}(0) + \Lambda^2 S_{12}(t)S_{12}(0) \rangle$ ,  $C_u(t) = \langle u_2(t)u_2(0) \rangle$  and  $C_X(t) = \langle u_2(t)[O_{12}(0) + |\Lambda|S_{12}] \rangle$ . For the statistical model, the correlation functions are given in the Supplemental Material. We remark that the average of the tilt angle and all higher odd-order moments must vanish, because positive and negative values of  $\text{sgn}(\delta\varphi)$  are equally likely,

Eq. (23) shows how translational particle inertia affects the tilt-angle variance. The flow-velocity correlations in Eq. (23) can be traced back to the effect of the fluctuating settling velocity due to particle inertia [first term on the r.h.s. of Eq. (19)]. The gradient correlations in Eq. (23) stem from the Jeffery torque (10), corresponding to the other two terms on the r.h.s. of Eq. (19).

Eq. (23) simplifies to (16) when translational inertia is negligible, in regime ② in Fig. 3. This can be seen by taking the limit  $\text{St}/A^{(g)} \rightarrow 0$  in Eq. (23). Using  $\frac{A^{(g)}}{\text{St}} e^{-tA^{(g)}/\text{St}} \sim 2\delta(t)$  gives

$$\langle \delta\varphi^2 \rangle \sim f_\Lambda \frac{\langle O_{12}^2 \rangle + \Lambda^2 \langle S_{12}^2 \rangle}{(|\mathcal{A}| \text{Sv}^2)^2}, \quad (24a)$$

for columns the same as Eq. (16). For platelets the variance is twice as large, consistent with the result of Anand et al. (2020). This difference in the prefactor between columns and platelets is a direct consequence of the different dynamics of  $\hat{p}$ .

In regimes ③ and ④, fluctuations of the translational slip velocity dominate. This follows from taking the limit  $\tau_\varphi \rightarrow 0$  in Eq. (23), where contributions from the fluid-velocity gradients disappear. We distinguish two cases.

First, in regime ③, we use  $\tau_\varphi \ll 1$  to simplify Eq. (23). Integration by parts, rescaling the integration variable with  $\tau_d$ , and using  $\tau_d \ll \tau_s \ll 1$  to expand the correlation functions gives:

$$\langle \delta\varphi^2 \rangle \sim f_\Lambda \frac{\text{St}^2}{A^{(g)2}} \langle A_{21}^2 \rangle. \quad (24b)$$

Eq. (24b) shows that the variance of the tilt angle forms an Sv-independent plateau in regime ③. In this regime the angular dynamics is overdamped. The St-dependence

is caused by fluctuations in the translational slip velocity, due to particle inertia.

Second, regime ④ corresponds to  $\tau_s \rightarrow 0$  at finite  $\tau_d = \text{St}/A^{(g)} \ll 1$ . Now the rotational dynamics is underdamped. Nevertheless, Equation Eq. (23) continues to hold, as demonstrated by the mean-field analysis described in Section II.C in the Supplemental Material.

Using the statistical-model correlation functions given in the Supplemental Material, we find:

$$\langle \delta\varphi^2 \rangle \sim f_\Lambda \frac{A^{(g)2}}{\text{Sv}^2} \langle u_2^2 \rangle. \quad (24c)$$

In dimensionless units, for homogeneous isotropic turbulent flows,  $\langle u_2^2 \rangle \approx \text{Re}_\lambda \approx \ell^2/\sqrt{15}$ . Accordingly, Eq. (24c) predicts that the tilt-angle variance is proportional to  $\text{Sv}^{-2}$  in regime ④. Finally, we can evaluate Eq. (23) in closed form for the statistical model, exhibiting how the variance depends on the dimensionless parameters  $\text{St}$ ,  $\text{Sv}$ , and  $\beta$  (details in the Supplemental Material).

Our time-scale analysis in Section 5 led to the phase diagram Fig. 3, describing the asymptotic behaviours of the tilt-angle variance. We obtain the same asymptotic boundaries by comparing the corresponding limits of our theory. For example, since  $\langle u_2^2 \rangle \sim \ell^2 \langle A_{21}^2 \rangle$ , Eqs. (24b) and (24c) are equal when  $\tau_s \sim \tau_d$ , the boundary between regimes ③ and ④. Similarly, Eqs. (24b) and (16) are equal when  $\tau_d \sim \tau_\varphi$ , i.e. the boundary between regimes ② and ③.

To obtain an asymptotic law in regime ④ we took the limit  $\text{Sv} \rightarrow \infty$ . It is important to note that the steady approximation for the convective-inertia torque breaks down when  $\mathbf{W}$  varies too rapidly (too large  $\text{Sv}$  gives too small  $\tau_s$ ). The model requires that  $\tau_s$  is much larger than the viscous time,  $a^2/\nu$ . We discuss this constraint further in Section 7.d.

Eq. (23) does not apply in regime ⑤ where both c.o.m. and angular dynamics are underdamped. The settling velocity is large ( $\tau_s$  is small). When  $\tau_s$  is the smallest time scale we approximate the  $\delta\varphi$ -dynamics as Langevin equations. Solving the corresponding Fokker-Planck equation for the moments of  $\delta\varphi$  we find in regime ⑤ for the statistical model:

$$\langle \delta\varphi^2 \rangle = f_\Lambda \frac{\sqrt{2\pi}}{60} |\mathcal{A}| A^{(g)} A^{(p)} \ell^3 \frac{A^{(g)}}{\text{Sv}} \quad (25)$$

(details in the Supplemental Material). The same caveat as for regime ④ applies: the settling time  $\tau_s$  must be larger than the viscous time  $a^2/\nu$ .

Fig. 4 shows how the tilt-angle variance depends on the particle aspect ratio, keeping  $\text{St}/A^{(g)}$  and  $\text{Sv}/A^{(g)}$  constant. The theoretical prediction (23) for regimes ② to ④ is shown for three different Stokes numbers (coloured solid lines). The overdamped approximation (16) is plotted as a black solid line. We see that it is accurate only in regime ②, for  $\beta$  approximately between 0.8 and 1.2 when

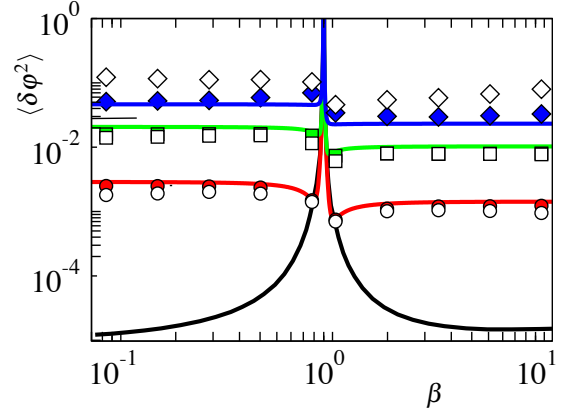


FIG. 4: Tilt-angle variance as a function of particle aspect ratio  $\beta$  keeping  $\text{St}/A^{(g)}$  and  $\text{Sv}/A^{(g)}$  constant. Results obtained using DNS of turbulence: empty symbols are with the inertial drag correction (12a), filled symbols without this correction. The overdamped approximation (16) is shown as a black solid line. Also shown is the theoretical prediction (23) for regimes ② to ④ for  $\ell = 14.7$ , coloured lines. Other parameters:  $\text{Sv}/A^{(g)} = 22$  and  $\text{St}/A^{(g)} = 0.11$  (red,  $\circ$ ), 0.45 (green,  $\square$ ), and 2.2 (blue,  $\diamond$ ).

$\text{St}/A^{(g)} = 0.11$ . For larger Stokes numbers this range is even narrower. Outside regime ②, particle inertia matters. We see that particle inertia increases the tilt-angle variance by a large factor compared to the overdamped approximation, by several orders of magnitude for slender columns and thin disks. Also, the tilt-angle variance is independent of  $\beta$ , unless  $\beta$  is close to unity. This follows from the fact that amongst all time scales in Table 2, only  $\tau_\varphi$  exhibits a significant  $\beta$  dependence at constant  $\text{Sv}/A^{(g)}$  and  $\text{St}/A^{(g)}$ . Since  $\tau_\varphi$  matters only in regime ②, it follows that the tilt-angle variance does not depend on  $\beta$  in regimes ③ and ④, as long as  $\text{Sv}/A^{(g)}$  and  $\text{St}/A^{(g)}$  are kept constant.

Also shown are results of numerical simulations of Eqs. (7) to (12) using DNS of turbulence. To maintain  $\tau_p/A^{(g)}$  constant, we adjusted the particle size as we changed  $\beta$ . We performed DNS with the inertial correction (12a) to the translational dynamics (empty symbols) and without (filled symbols). The Reynolds number was  $\text{Re}_\lambda \approx 56$ . For the comparison with the theory we identified  $\ell$  with the Taylor scale and used, in dimensional variables,  $\lambda/\eta_K = 15^{1/4} \sqrt{\text{Re}_\lambda} \approx 14.7$ .

Figure 4 demonstrates that our theory (23) describes the DNS results very well, without any fitting parameter. For the smaller Stokes numbers [ $\text{St}/A^{(g)} = 0.11$  (circles) and 0.45 (squares)], the inertial correction (12a) to the translational dynamics is quite small, except at very small and very large values of  $\beta$  – where  $\text{Re}_p$  is largest. A simple order-of-magnitude estimate explains that the Oseen correction (12a) has only a small effect on  $\langle (\delta\varphi)^2 \rangle$  for the parameters considered here (Gustavsson et al. 2019): the

inertial correction is smaller than the Stokes force (9) by the small factor  $a/\eta_K$ .

Looking in more detail, we infer from Fig. 4 that the Oseen correction appears to decrease the tilt-angle variance somewhat in regimes ②, ③, and ④. This is explained by the fact that the Oseen correction increases the translational drag and therefore reduces the slip-velocity fluctuations. Yet the difference remains small for the parameters in Fig. 4, as mentioned above.

The data for the largest Stokes number agrees less well with Eq. (23). This is expected because the values  $St/A^{(g)} = 2.2$  and  $Sv/A^{(g)} = 22$  lie near the boundary to regime ⑤ where Eq. (23) begins to fail (the Stokes number is not yet large enough for Eq. (25) to work).

We also see that the inertial correction (12a) to the translational dynamics makes a substantial difference in regime ⑤, where the tilt-angle variance is much larger when the drag correction is included. In part this can be attributed to a larger particle Reynolds number, but in regime ⑤ we do not understand the effect of the correction (12a) in detail.

## 7. Discussion

### a. Comparison with Klett's theory

The main assumptions underlying Eq. (1) are that translational particle inertia is negligible, that the particles are nearly spherical, and that the driving of the angular dynamics is white noise.

The time-scale analysis in Section 5 says that translational inertia can only be neglected in regimes ① and ②. In regime ①, the inertial alignment torque is negligible ( $\tau_\varphi \gg 1$ ). Therefore this discussion concentrates on the case  $\tau_\varphi \ll 1$ , where not only translational but also rotational inertia is negligible.

In Fig. 3 we stipulated that  $\tau_s \ll \tau_d$  in regime ②. But for nearly spherical particles, as considered by Klett, one can have  $\tau_d \ll \tau_s$ , so that  $\tau_d \ll \tau_s \ll \tau_\varphi \ll 1$ . In this limit,  $\tau_d$  is the smallest time scale. Therefore the dynamics is overdamped as in regime ②. But since  $\tau_s \ll \tau_\varphi$ , the fluid-velocity gradients vary more rapidly than the inertial torque. Therefore they can be approximated by white noise, as assumed by Klett. Using the asymptotic forms of the resistance coefficients for nearly spherical particles, we find that the condition  $\tau_d \ll \tau_s$  is difficult to satisfy, it requires  $\sqrt{4480/811} \ll Sv|\beta - 1| \ll 4480/(811\ell)$ .

In this white-noise limit we obtain that  $\langle \delta\varphi^2 \rangle \sim Sv^{-3}$ . This result differs from Eq. (1) by a factor of  $Sv^{-1}$ . The missing factor comes from the fact that the time scale of the fluid-velocity gradients is  $\tau_s$  for large  $Sv$ , not  $\tau_K$ . As a consequence the variance catches the additional factor  $Sv^{-1}$ .

In regime ④, on the other hand, the tilt-angle variance is proportional to  $Sv^{-2}$  in the statistical model, just

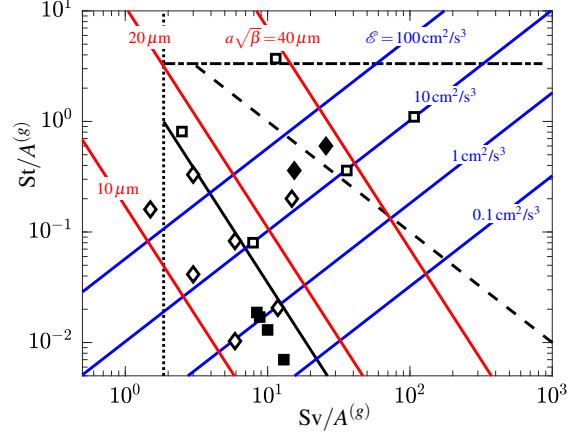


FIG. 5: Phase diagram, similar to Fig. 3 for platelet-shaped crystals, for  $\ell = 10$ . Symbols show the values of the dimensionless parameters corresponding to experimental and numerical studies of non-spherical crystals settling in turbulence (details in Supplemental Material). Dimensionless parameters estimated from: (Bréon and Dubrulle 2004) ( $\square$ ); numerical study of collisions between disks settling in turbulence (Jucha et al. 2018) ( $\diamond$ ); experiments by Kramel (2017) ( $\blacksquare$ ), and Esteban et al. (2020) ( $\blacklozenge$ ). Blue solid lines show contours of constant turbulent dissipation rate,  $\mathcal{E} = 0.1, 1, 10, 100 \text{ cm}^2/\text{s}^3$ , using Eq. (26) with  $v = 0.1 \text{ cm}^2/\text{s}$ ,  $\rho_p/\rho_f = 1000$ , and  $g = 980 \text{ cm/s}^2$ . Red solid lines show contours of constant  $a\sqrt{\beta} = 10, 20, 40 \mu\text{m}$  (see text).

like Eq. (1). But the angular dynamics is driven by slip-velocity fluctuations, the Jeffery torque (10) does not matter. This leads to a different parameter dependence of the prefactor. In dimensional variables, our statistical-model result for regime ④ [Eq. (24c)] reads  $\langle \delta\varphi^2 \rangle \sim \text{Re}_\lambda \sqrt{\mathcal{E}v}/W^2$ .

In summary there are three difficulties with Eq. (1). First, it accounts for particle inertia in the angular dynamics but not for translational particle inertia. Our analysis shows that translational particle inertia cannot be neglected in general, only if also rotational inertia is negligible. Second, Eq. (1) assumes that the stochastic driving is isotropic white noise. When  $\tau_d \ll \tau_s$ , the fluid-velocity gradients seen by the particle can be approximated by white noise, but their diffusion time scale is given by  $\tau_s$ , not  $\tau_K$ . Third, this white-noise limit is difficult to achieve unless  $\beta$  is close to unity.

### b. Estimates of dimensionless parameters

Parameter values for different experimental and theoretical studies of non-spherical, platelet-shaped crystals settling in turbulence are shown in Fig. 5. Note that the locations of the boundaries  $\tau_\varphi = 1$  and  $\tau_\varphi = \tau_d$  depend on  $\beta$ , but only weakly unless  $\beta$  is close to unity. The boundaries

are drawn for  $\beta = 0.1$  in Fig. 5, but for slender platelets the precise value of the aspect ratio does not matter as far as the phase boundaries are concerned.

The boundaries of regimes ② and ④ are affected by the value of the turbulent Reynolds number  $\text{Re}_\lambda$ , because it determines the correlation length  $\ell$ , as explained above. Since  $\tau_s$  depends on  $\ell$ , a larger value of  $\ell$  restricts regime ④ to yet larger values of  $\text{Sv}$ . Moreover, since  $\langle u_2^2 \rangle \sim \ell^2 \langle A_{21}^2 \rangle$ , a larger value of  $\ell$  reduces the prefactor of the result in regime ②, where flow-gradients dominate, compared to the result in regime ③, where the fluid velocity dominates. It is likely that  $\ell$  is of the same order for the different data sets, but not the same. We simply set  $\ell = 10$  in Fig. 5.

Which values of the dimensionless parameters  $\text{St}$  and  $\text{Sv}$  are relevant for ice-crystal platelets in clouds? Both  $\text{Sv}$  and  $\text{St}$  are proportional to  $\tau_p$ , see Table 1, which in turn depends on the size and the shape of the platelet through the product  $a\sqrt{\beta}$ , on the turbulent energy dissipation rate  $\mathcal{E}$ , as well as upon the fluid viscosity  $\nu$ , mass-density ratio  $\rho_p/\rho_f$ , and the gravitational acceleration  $g$ . Using typical values for ice crystals in clouds,  $\nu \approx 0.1 \text{ cm}^2/\text{s}$ ,  $\rho_p/\rho_f \approx 1000$ , and  $g \approx 980 \text{ cm/s}^2$ , we can express  $\text{St}$  and  $\text{Sv}$  in terms of the dimensional parameter combinations  $\mathcal{E}$  and  $a\sqrt{\beta}$  as:

$$\text{St} \approx 8200 (a\sqrt{\beta})^2 \sqrt{\mathcal{E}} \quad \text{and} \quad \text{Sv} \approx 0.0018 \mathcal{E}^{3/4} \text{St}. \quad (26)$$

Fig. 5 shows four blue lines corresponding to fixed values of turbulence intensity  $\mathcal{E}$ , covering the range observed in clouds (Grabowski and Vaillancourt 1999), and three red lines at three fixed values of  $a\sqrt{\beta}$  (for platelets this is the only dependence on the value of  $\beta$  because  $A^{(g)}$  is approximately constant for  $\beta < 0.1$ ,  $A^{(g)} \approx 0.85$ , see Table S1 in the Supplemental Material).

We took parameter values relevant to platelets settling in turbulent flows from Bréon and Dubrulle (2004); Jucha et al. (2018), empty symbols in Fig. 5. The corresponding Stokes number ranges from  $\text{St}/A^{(g)} \approx 10^{-2}$  to 3, and the settling number ranges from  $\text{Sv}/A^{(g)} \approx 1$  to 100. So the first conclusion of our analysis is that particle inertia matters in a large range of the parameter space, not only for platelets settling in clouds, but also for other experiments: Fig. 5 also shows values of  $\text{St}$  and  $\text{Sv}$  from recent experiments measuring non-spherical particles settling in turbulent water (Kramel 2017; Esteban et al. 2020).

Note also that the lines of constant  $a\sqrt{\beta}$  in Fig. 5 are parallel, in the log-log representation of the Figure, to the phase boundary between regimes ② and ③. Therefore only the smallest platelets, with  $a\sqrt{\beta} \ll 18 \mu\text{m}$ , exhibit overdamped dynamics (regime ②).

In conclusion, many of the relevant parameter values lie in the centre of the parameter plane where the different asymptotic regions meet. In these cases, the tilt-angle variance is determined by a combination of different mechanisms, and we do not expect its dependence upon the

settling velocity or particle size to be of power-law form. This is the second main conclusion of our analysis.

### c. Comparison with observations

Our analysis shows how the tilt angle depends on particle size and on the turbulent dissipation rate  $\mathcal{E}$ . The results shown in Fig. 3 indicate that the tilt angle depends quite weakly upon particle shape  $\beta$  at constant  $\text{St}/A^{(g)}$  and  $\text{Sv}/A^{(g)}$ .

Observations (Noel and Chepfer 2004; Noel and Sassen 2005) indicate that crystals settling in cirrus clouds align very well, with fluctuations  $\langle \delta\varphi^2 \rangle^{1/2}$  no larger than  $\approx 1^\circ$ , or equivalently  $\log_{10} \langle \delta\varphi^2 \rangle < -3.5$ . Our Fig. 3 shows that such small values of  $\langle \delta\varphi^2 \rangle$  can only occur at very small turbulence intensities, of the order of  $\mathcal{E} \sim 1 \text{ cm}^2/\text{s}^3$  or smaller. Available measurement of the kinematic energy dissipation in cirrus clouds is consistent with this conclusion: values in the range  $0.1 - 1 \text{ cm}^2/\text{s}^3$  are observed in such clouds (Gultepe and Starr 1995; Westbrook et al. 2010).

Fig. 9 of Bréon and Dubrulle (2004) indicates that typical tilt angles of quite large ice-crystal platelets ( $a \sim 1 \text{ mm}$ ) at reasonably high cloud-turbulence levels, with  $\mathcal{E} \sim 1000 \text{ cm}^2/\text{s}^3$ , are of the order of a few degrees. Our model (Fig. 4) predicts that the variance ranges from  $\langle \delta\varphi^2 \rangle \sim 10^{-3} \text{ rad}^2$  for small Stokes numbers to  $\sim 0.1 \text{ rad}^2$  for larger Stokes numbers, corresponding to typical tilt angles between 2 and 18 degrees. So at larger Stokes numbers our model gives a much higher tilt-angle than the average estimated by Bréon and Dubrulle (2004). Thus, contrary to the predictions of Cho et al. (1981), our results point to a strong effect of turbulence upon alignment. How can our estimate for the tilt-angle variance be reconciled with the much smaller one of Bréon and Dubrulle (2004)? One possibility is that crystals strongly align only in regions where the turbulence intensity is much weaker. This might explain the relatively low fraction of crystals observed to align. Another possibility is that our model becomes inaccurate for the relatively large crystals considered by Bréon and Dubrulle (2004). We discuss the limitations of the model next.

### d. Limitations of the model

The model equations assume that  $\text{Re}_p$  remains small, because we neglected  $\text{Re}_p$ -corrections to the c.o.m. dynamics and considered only the lowest-order  $\text{Re}_p$ -expression for the convective inertial torque, assuming that  $\text{Re}_p$  is less than unity. The parameter values of Bréon and Dubrulle (2004) corresponding to the largest Stokes numbers have particle Reynolds numbers larger than 10, and the experiments of Esteban et al. (2020) correspond to still larger particle Reynolds numbers (all parameter values are summarised in the Supplemental Material). In our numerical computations using DNS of turbulence we kept the

linear  $Re_p$ -corrections to the c.o.m. dynamics. The results indicate that these corrections do not make a qualitative difference in regimes ②, ③, and ④, for the chosen parameters. At large Stokes numbers (in regime ⑤), by contrast, our simulations show that the correction (12a) can make a substantial difference. At present we do not know how to describe this effect in regime ⑤.

Higher-order  $Re_p$ -corrections to the convective inertial torque are known in closed form only for slender columns (Khayat and Cox 1989; Lopez and Guazzelli 2017). Jiang et al. (2021) quantified how well Eq. (12b) works at larger  $Re_p$ , for spheroids in a steady homogeneous flow. For particle Reynolds numbers up to  $Re_p$  of the order of 10 the angular dependence remains accurate, but the numerical prefactor is smaller than predicted by Eq. (12b). In regime ② this leads to a larger variance. In regime ⑤, by contrast, Eq. (25) implies that the tilt-angle variance decreases, at least when the statistical model applies. In regimes ③ and ④ it is less clear what happens, because the asymptotic expressions (24b) and (24c) are independent of the inertial-torque amplitude  $\mathcal{A}$ . Finally, smaller values of the torque imply that the condition  $\tau_\phi \sim 1$ , which defined the transition from regime ①, is shifted to higher values of  $Sv$ , extending the parameter range where the tilt angle is uniformly distributed.

As  $Re_p$  increases, the dynamics of disks settling in a quiescent fluid becomes unstable (Auguste et al. 2013; Esteban et al. 2020), because the symmetry of the disturbance flow is broken, and because it becomes unsteady. Our model cannot describe these effects due to fluid inertia.

The model uses a steady approximation for the convective inertial torque (Kramel 2017; Menon et al. 2017; Lopez and Guazzelli 2017; Gustavsson et al. 2019; Sheikh et al. 2020). The experiments by Lopez and Guazzelli (2017) indicate that this is at least qualitatively correct for rods settling in a cellular flow, although the slip velocity  $\mathbf{W}(t)$  fluctuates as a function of time. In general, however, the steady model must break down when  $\mathbf{W}(t)$  fluctuates too rapidly (Candelier et al. 2019). For the steady model to hold in our case, it is necessary that  $\tau_s$  is much larger than the viscous time,  $\tau_s \gg a^2/\nu$  (in this Section we use dimensional variables). Otherwise unsteady effects may arise, analogous to the Basset-Boussinesq-Oseen history force for the c.o.m. motion of a sphere in a quiescent fluid. For the cellular flow with correlation length  $\ell$  (Lopez and Guazzelli 2017) we require  $\ell/W \gg a^2/\nu$ . Using  $Re_p = Wa/\nu$  this means  $\ell/(Re_p a) \gg 1$ . In the experiments,  $\ell \sim 1$  cm,  $a \sim 1$  mm, and the largest Reynolds number is  $Re_p \sim 10$ . So the condition is marginally satisfied for the largest  $Re_p$ . In the statistical model, using  $\tau_s/\tau_K = (A^{(g)}/Sv)(\ell/\eta_K)$  (in dimensional variables), the condition translates to  $Sv \ll A^{(g)}\ell\eta_K/a^2$ , consistent with the constraint (5).

The model also neglects the convective-inertial torque due to fluid shears (Subramanian and Koch 2005; Einarsson et al. 2015; Rosén et al. 2015). This is justified if  $a/\eta_K \ll 1$  (Candelier et al. 2016), but for larger particles the shear-induced torque might matter. This torque has a different physical origin from the convective-inertial torque due to finite slip. The former is determined by the disturbance flow close to the particle, while the latter is due to far-field effects, where the presence of the particle is approximately taken into account by a singular source term. As a first approximation, one could therefore simply superimpose the torques due to shear and due to slip.

Our model assumes that the ice crystals are homogeneous, in other words that the mass density is the same throughout the crystal. With this constraint, the choice of model parameters is overall consistent with known properties of ice crystals in clouds. The values of  $\beta$  chosen in Fig. 5 for crystals of diameter  $300\mu\text{m}$  (empty diamond symbols),  $0.01 \leq \beta \leq 0.05$ , lead to settling velocities consistent with those reported in laboratory studies (Kajikawa 1972; Pruppacher and Klett 1997). The empty square symbols are taken from the study of Bréon and Dubrulle (2004), and also correspond to realistic settling velocity of crystals, consistent with known results (Auer and Veal 1970; Heymsfield 1972).

In reality, the microscopic growth processes of cloud crystals may result in inhomogeneous mass densities (Heymsfield 1973). The crystals may even contain hollow regions and may exhibit irregular shapes (Korolev et al. 2000; Heymsfield et al. 2002a). How such imperfections affect the dynamics of ice crystals is not considered in our model. An inhomogeneous mass distribution results in an additional gravitational torque which could affect the angular dynamics. This is well studied for nearly neutrally buoyant marine microorganisms settling in the turbulent ocean (Kessler 1985; Durham et al. 2013; Gustavsson et al. 2016), but little is known for heavy particles settling in air. Shape irregularities can affect the inertial contribution to the torque (Khayat and Cox 1989; Candelier and Mehlig 2016). The highly idealised model of Candelier and Mehlig (2016) shows that such asymmetries have a negligible effect on the dynamics of slender columns if  $\delta a_\perp/a_\perp \ll \beta Re_p$ , their Eq. (4.11). The experiments and the refined analysis of Roy et al. (2019) bear out this qualitative prediction. Conversely, if  $\delta a_\perp/a_\perp \gg \beta Re_p$ , then the asymmetry dominates the angular dynamics. Slender columns settle vertically in this limit, aligned with gravity. This is not observed for columnar crystals in clouds.

## 8. Conclusions

Particle inertia increases the tilt-angle variance of small crystals settling through a turbulent cloud because it gives rise to additional fluctuations in the angular equation of motion. Even at very small Stokes numbers this can be

a significant effect, since the overdamped theory (Kramel 2017; Menon et al. 2017; Gustavsson et al. 2019; Anand et al. 2020) predicts a very small variance. For neutrally buoyant particles the overdamped theory works fairly well. But for ice crystals that are about 1000 times heavier than air it can underestimate the variance by a large factor. Moreover, we found that particle inertia matters in a large region in parameter space (Fig. 5).

The problem has four relevant time scales (Table 2). As a consequence there are many different asymptotic regimes where the tilt-angle variance displays different dependencies on the dimensionless parameters (Table 1), in particular different power laws as a function of the settling number  $S_v$ . Relevant dimensionless parameters tend to lie in a central region in the parameter plane where the different asymptotic regimes meet, so that the tilt-angle variance is determined by a combination of different physical mechanisms. In this case there are no simple power-law dependencies on the settling velocity [Eqs. (1) or (2)].

Our results are based on a small-angle expansion, as first used by Klett (1995) for this problem. Other assumptions of his theory are not satisfied in the regimes we studied, so that its main prediction (1) does not describe our simulation results.

Our analysis shows that the very strong alignment of ice crystals in cirrus clouds, with typical tilt angles  $\langle \varphi^2 \rangle^{1/2} \sim 1^\circ$  or less (Noel and Chepfer 2004; Noel and Sassen 2005) is only possible when the turbulence intensity is low, of the order of  $0.1 - 1 \text{ cm}^2/\text{s}^3$ . This is generally consistent with the known value of turbulent energy dissipation rate in such ice clouds (Gultepe and Starr 1995). In fact, an important future test of our theory is to correlate the presence of strongly oriented ice crystal (Noel and Chepfer 2010) with the local level of cloud turbulence. Another test is to calculate what a satellite sensor would detect, starting from the size distribution of either columns or platelets obtained by aircraft observations (Heymsfield et al. 2002a), together with estimates of local cloud-turbulence levels.

Such tests are important because the model was derived under a number of assumptions. First, we assumed that the particle Reynolds number is small. Second, we assumed that the torque is obtained by simply superimposing the fluid-inertia torque and the Jeffery torque. But as we discussed, there are additional contributions to the torque when turbulent shears give rise to convective fluid inertia. For crystals smaller than the Kolmogorov length, these contributions are negligible because the shear Reynolds number is small (Candelier et al. 2016), but for larger crystals they may become important. Third, Eq. (12b) was derived in the steady limit. For the steady model to hold it is necessary that the fluctuations of the slip velocity are slow compared with the viscous time. At very large settling numbers this constraint is broken. It remains a question for the future to describe the effect of unsteady torques.

In our discussion of the results we focused on the variance of the tilt angle  $\varphi$ , the angle between the particle-symmetry vector and the direction of gravity. But to compute the effect of particle inertia we needed to consider a second angle,  $\theta$ , that describes how the particle-symmetry vector rotates in the plane perpendicular to the direction of gravity. Regarding the dynamics of  $\theta$  we found significant differences between columns and platelets, described in the Supplemental Material. For the tilt-angle variance these differences do not matter much, but they are likely to be important for collisions between ice crystals, a question that remains to be explored (Sheikh et al. 2021).

We remark that although this study focused on the variance of the tilt angle, the method leading to Eq. (23) and outlined in the Supplemental Material, can straightforwardly be extended to calculate higher-order moments or correlation functions of the tilt angle.

When particle inertia becomes important, preferential sampling may affect the statistics of observables such as the tilt angle. This is well known for heavy spherical particles in turbulence (Gustavsson and Mehlig 2016). Our results show that preferential sampling is a weak effect, at least for the parameters considered here.

Finally, we assumed that the particles are much heavier than the fluid, this is the limit relevant for ice crystals in clouds. But recent experimental studies (Kramel 2017; Lopez and Guazzelli 2017) used nearly neutrally buoyant particles. In this case one expects the effect of particle inertia to be weaker. It remains an open question under which circumstances particle inertia may nevertheless make a noticeable difference.

*Acknowledgments.* BM thanks Fabien Candelier for discussions regarding the inertial torque. KG and BM were supported by the grant *Bottlenecks for particle growth in turbulent aerosols* from the Knut and Alice Wallenberg Foundation, Dnr. KAW 2014.0048, and in part by VR grant no. 2017-3865 and Formas grant no. 2014-585. AP and AN acknowledge support from the IDEXLYON project (Contract ANR-16-IDEX-0005) under University of Lyon auspices. Computational resources were provided by C3SE and SNIC, and PSMN.

## References

- Anand, P. S., S. S. Ray, and G. Subramanian, 2020: Orientation dynamics of sedimenting anisotropic particles in turbulence. *Phys. Rev. Lett.*, **125**, 034 501.
- Auer, A. H., and D. L. Veal, 1970: The dimension of ice crystals in natural clouds. *Journal of the Atmospheric Sciences*, **27** (6), 919–926, doi:10.1175/1520-0469(1970)027<0919:tdoici>2.0.co;2.
- Auguste, F., J. Magnaudet, and D. Fabre, 2013: Falling styles of disks. *Journal of Fluid Mechanics*, **719**, 388–405.
- Baran, A. J., 2012: From the single-scattering properties of ice crystals to climate prediction: A way forward. *Atmos. Res.*, **112**, 45–69.

- Brenner, H., 1961: The Oseen resistance of a particle of arbitrary shape. *J. Fluid Mech.*, **11**, 604–610.
- Bréon, F.-M., and B. Dubrulle, 2004: Horizontally oriented plates in clouds. *Journal of the Atmospheric Sciences*, **61**, 2888–2898.
- Bretherton, F., 1962: The motion of rigid particles in a shear flow at low Reynolds number. *J. Fluid Mech.*, **14** (02), 284–304.
- Candelier, F., J. Einarsson, and B. Mehlig, 2016: Rotation of a small particle in turbulence. *Phys. Rev. Lett.*, **117**, 204 501.
- Candelier, F., and B. Mehlig, 2016: Settling of an asymmetric dumbbell in a quiescent fluid. *J. Fluid Mech.*, **802**, 174–185.
- Candelier, F., B. Mehlig, and J. Magnaudet, 2019: Time-dependent lift and drag on a rigid body in a viscous steady linear flow. *Journal of Fluid Mechanics*, **864**, 554–595.
- Chen, J. P., and D. Lamb, 1994: The theoretical basis for the parametrization of ice crystal habits: Growth by vapor deposition. *J. Atmos. Sci.*, **51**, 1206–1222.
- Cho, H.-R., J. V. Iribarne, and W. G. Richards, 1981: On the orientation of ice crystals in a cumulonimbus cloud. *J. Atmos. Sci.*, **38**, 1111.
- Cox, R., 1965: The steady motion of a particle of arbitrary shape at small Reynolds numbers. *J. Fluid Mech.*, **23**, 625–643.
- Dabade, V., N. K. Marath, and G. Subramanian, 2015: Effects of inertia and viscoelasticity on sedimenting anisotropic particles. *J. Fluid Mech.*, **778**, 133–188.
- Devenish, B. J., and Coauthors, 2012: Droplet growth in warm turbulent clouds. *Q. J. R. Meteorol. Soc.*, **138**, 1401–1429.
- Durham, W. M., E. Climent, M. Barry, F. D. Lillo, G. Boffetta, M. Cencini, and R. Stocker, 2013: Turbulence drives microscale patches of motile phytoplankton. *Nature Communications*, **4**, 2148.
- Einarsson, J., F. Candelier, F. Lundell, J. Angilella, and B. Mehlig, 2015: Rotation of a spheroid in a simple shear at small Reynolds number. *Phys. Fluids*, **27**, 063301.
- Esteban, L. B., J. S. Shrimpton, and B. Ganapathisubramani, 2020: Disks settling in turbulence. *Journal of Fluid Mechanics*, **883**, A58.
- Fries, J., J. Einarsson, and B. Mehlig, 2017: Angular dynamics of small crystals in viscous flow. *Phys. Fluids*, **2**, 014 302.
- Grabowski, W. W., and P. Vaillancourt, 1999: Comments on ‘Preferential Concentration of Cloud Droplets by Turbulence: Effects on the Early Evolution of Cumulus Cloud Droplet Spectra’. *Journal of the Atmospheric Sciences*, **56** (10), 1433–1436.
- Gultepe, I., and D. O. Starr, 1995: Dynamical structure and turbulence in cirrus clouds. *J. Atmos. Sci.*, **52**, 4159–4182.
- Gustavsson, K., F. Berglund, P. R. Jonsson, and B. Mehlig, 2016: Preferential sampling and small-scale clustering of gyrotactic microswimmers in turbulence. *Phys. Rev. Lett.*, **116**, 108 104.
- Gustavsson, K., J. Jucha, A. Naso, E. Lévêque, A. Pumir, and B. Mehlig, 2017: Statistical model for the orientation of nonspherical particles settling in turbulence. *Phys. Rev. Lett.*, **119**, 254 501.
- Gustavsson, K., and B. Mehlig, 2016: Statistical models for spatial patterns of heavy particles in turbulence. *Adv. Phys.*, **65**, 1.
- Gustavsson, K., M. Z. Sheikh, D. Lopez, A. Naso, A. Pumir, and B. Mehlig, 2019: Theory for the effect of fluid inertia on the orientation of a small spheroid settling in turbulence. *New J. Phys.*, **21**, 083 008.
- Heymsfield, A., 1972: Ice crystal terminal velocities. *Journal of the Atmospheric Sciences*, **29** (7), 1348–1357, doi:10.1175/1520-0469(1972)029<1348:ictv>2.0.co;2.
- Heymsfield, A. J., 1973: Laboratory and field observations of the growth of columnar and plate crystals from frozen droplets. *J. Atmos. Sci.*, **30**, 1650–1656.
- Heymsfield, A. J., A. Bansemer, P. R. Field, S. L. Durden, J. L. Stith, J. E. Dye, W. Hall, and C. A. Granigner, 2002a: Observations and parameterizations of particle size distributions in deep tropical cirrus and stratiform precipitating clouds: results from in situ observations in TRMM field campaigns. *Journal of the Atmospheric Sciences*, **59**, 3457–3491.
- Heymsfield, A. J., S. Lewis, A. Bansemer, J. Iaquinta, L. M. Miloshevich, M. Kajikawa, C. Twohy, and M. R. Poellot, 2002b: A general approach for deriving the properties of cirrus and stratiform ice cloud particles. *Journal of the Atmospheric Sciences*, **59**, 3–29.
- Jeffery, G. B., 1922: The motion of ellipsoidal particles immersed in a viscous fluid. *Proc. R. Soc. A*, **102**, 161.
- Jiang, F., L. Zhao, H. Andersson, K. Gustavsson, A. Pumir, and B. Mehlig, 2021: Inertial torque on a small spheroid in a stationary uniform flow. *Phys. Rev. Fluids*.
- Jucha, J., A. Naso, E. Lévêque, and A. Pumir, 2018: Settling and collision between small ice crystals in turbulent flows. *Phys. Rev. Fluids*, **3**, 014 604.
- Kajikawa, M., 1972: Measurement of falling velocity of individual snow crystals. *Journal of the Meteorological Society of Japan. Ser. II*, **50** (6), 577–584, doi:10.2151/jmsj1965.50.6.577.
- Kessler, J. O., 1985: Hydrodynamic focusing of motile algal cells. *Nature*, **313**, 218–220.
- Khayat, R., and R. Cox, 1989: Inertia effects on the motion of long slender bodies. *J. Fluid Mech.*, **209**, 435–462.
- Kim, S., and S. J. Karrila, 1991: *Microhydrodynamics: principles and selected applications*. Butterworth-Heinemann, Boston.
- Klett, J. D., 1995: Orientation model for particles in turbulence. *J. Atmospheric Sci.*, **52**, 2276–2285.
- Korolev, A., G. A. Isaac, and J. Hallett, 2000: Ice particle habits in stratiform clouds. *Q. J. R. Meteorol. Soc.*, **126**, 2873–2902.
- Kramel, S., 2017: Non-spherical particle dynamics in turbulence. Ph.D. thesis, Wesleyan University.
- Lopez, D., and E. Guazzelli, 2017: Inertial effects on fibers settling in a vortical flow. *Phys. Rev. Fluids*, **2**, 024 306.
- Magono, C., and C. W. Lee, 1966: Meteorological classification of natural snow crystals. *Journal of the Faculty of Science, Hokkaido University. Series 7, Geophysics*, **2** (4), 321–335.
- Menon, U., A. Roy, S. Kramel, G. Voth, and D. Koch, 2017: Theoretical predictions of the orientation distribution of high-aspect-ratio, inertial particles settling in isotropic turbulence. *Abstract Q36.00011, 70th Annual Meeting of the APS Division of Fluid Dynamics, Denver, Colorado*.

- Naso, A., J. Jucha, E. L ev eque, and A. Pumir, 2018: Collision rate of ice crystals with water droplets in turbulent flows. *Journal of Fluid Mechanics*, **845**.
- Noel, V., and H. Chepfer, 2004: Study of ice crystal orientation in cirrus clouds based on satellite polarized radiance measurements. *Journal of the Atmospheric Sciences*, **61** (16), 2073–2081, doi:10.1175/1520-0469(2004)061<2073:soicoi>2.0.co;2.
- Noel, V., and H. Chepfer, 2010: A global view of horizontally oriented crystals in ice clouds from cloud-aerosol lidar and infrared pathfinder satellite observation (CALIPSO). *Journal of Geophysical Research*, **115**, doi:10.1029/2009jd012365.
- Noel, V., H. Chepfer, M. Haefelin, and Y. Morille, 2006: Classification of ice crystal shapes in midlatitude ice clouds from three years of lidar observations over the sirta observatory. *Journal of the Atmospheric Sciences*, **63**, 2978–2991.
- Noel, V., and K. Sassen, 2005: Study of planar ice crystal orientations in ice clouds from scanning polarization lidar observations. *Journal of Applied Meteorology*, **44** (5), 653–664, doi:10.1175/jam2223.1.
- Pruppacher, H. R., and J. D. Klett, 1997: *Microphysics of clouds and precipitation, 2nd edition*. Kluwer Academic Publishers, Dordrecht, The Netherlands, 954p.
- Ros en, T., J. Einarsson, A. Nordmark, C. K. Aidun, F. Lundell, and B. Mehlig, 2015: Numerical analysis of the angular motion of a neutrally buoyant spheroid in shear flow at small reynolds numbers. *Phys. Rev. E*, **92**, 063 022, doi:10.1103/PhysRevE.92.063022, URL <https://link.aps.org/doi/10.1103/PhysRevE.92.063022>.
- Roy, A., R. J. Hamati, L. Tierney, D. L. Koch, and G. A. Voth, 2019: Inertial torques and a symmetry breaking orientational transition in the sedimentation of slender fibres. *Journal of Fluid Mechanics*, **875**, 576–596.
- Sassen, K., 1980: Remote sensing of planar ice crystal fall attitudes. *Journal of the Meteorological Society of Japan. Ser. II*, **58** (5), 422–429, doi:10.2151/jmsj1965.58.5\_422.
- Sassen, K., 1991: The polarization lidar technique for cloud research: A review and current assessment. *Bulletin of the American Meteorological Society*, **72** (12), 1848–1866, doi:10.1175/1520-0477(1991)072<1848:tpltfc>2.0.co;2.
- Sassen, K., and S. Benson, 2001: A midlatitude cirrus cloud climatology from the facility for atmospheric remote sensing. part II: Microphysical properties derived from lidar depolarization. *Journal of the Atmospheric Sciences*, **58** (15), 2103–2112, doi:10.1175/1520-0469(2001)058<2103:amcccf>2.0.co;2.
- Sheikh, M. Z., K. Gustavsson, D. Lopez, E. Leveque, B. Mehlig, A. Pumir, and A. Naso, 2020: Importance of fluid inertia for the orientation of spheroids settling in turbulent flow. *J. Fluid Mech.*, **886**, A9.
- Sheikh, M. Z., K. Gustavsson, D. Lopez, E. Leveque, B. Mehlig, A. Pumir, and A. Naso, 2021: Collision between small ice crystals in turbulent flows: effect of fluid inertia.
- Siewert, C., R. P. J. Kunnen, M. Meinke, and W. Schr oder, 2014a: Orientation statistics and settling velocity of ellipsoids in decaying turbulence. *Atmos. Res.*, **142**, 45–56.
- Siewert, C., R. P. J. Kunnen, and W. Schr oder, 2014b: Collision rates of small ellipsoids settling in turbulence. *J. Fluid Mech.*, **758**, 686–701.
- Subramanian, G., and D. L. Koch, 2005: Inertial effects on fibre motion in simple shear flow. *Journal of Fluid Mechanics*, **535**, 383–414, doi:10.1017/S0022112005004829.
- Westbrook, C. D., A. J. Illingworth, E. J. O’Connor, and R. J. Hogan, 2010: Doppler lidar measurement of oriented planar ice crystals falling from supercooled and glaciated layer clouds. *Q. J. R. Meteorol. Soc.*, **29** (136), 260–276, doi:10.1175/1520-0469(1972)029<1348:ictv>2.0.co;2.
- Yang, P., L. Bi, B. A. Baum, K.-N. Liou, G. W. Kattawar, M. I. Mishchenko, and B. Cole, 2013: Spectrally consistent scattering, absorption, and polarization properties of atmospheric ice crystals at wavelengths from 0.2 to 100  $\mu\text{m}$ . *Journal of the Atmospheric Sciences*, **70** (1), 330–347, doi:10.1175/jas-d-12-039.1.

# Supplemental Material for ‘Effect of particle inertia on the alignment of small ice crystals in turbulent clouds’

K. Gustavsson<sup>1</sup>, M. Z. Sheikh<sup>2</sup>, A. Naso<sup>3</sup>, A. Pumir<sup>2</sup>, B. Mehlig<sup>1</sup>

<sup>1</sup> *Department of Physics, Gothenburg University, 41296 Gothenburg, Sweden*

<sup>2</sup> *Univ. Lyon, ENS de Lyon, Univ. Claude Bernard, CNRS, Laboratoire de Physique, F-69342, Lyon, France*

<sup>3</sup> *Univ. Lyon, Ecole Centrale de Lyon, Univ. Claude Bernard, CNRS, INSA de Lyon, Laboratoire de Mécanique des Fluides et d’Acoustique, F-69134, Ecully, France*

## I. RESISTANCE AND INERTIA TENSORS FOR A SPHEROID

For a spheroid, the resistance tensors in Eqs. (9) and (10) in the main text, and the particle inertia tensor in Eq. (8) are given by Kim and Karrila (1991). For convenience we summarise the relevant formulae in this Section. The translational resistance tensor  $\mathbb{A}$  of a spheroid reads

$$A_{ij} \equiv A_{\perp}(\delta_{ij} - n_i n_j) + A_{\parallel} n_i n_j, \quad (\text{S1})$$

with coefficients

$$A_{\perp} = \frac{8(\beta^2 - 1)}{3\beta[(2\beta^2 - 3)\gamma + 1]}, \quad A_{\parallel} = \frac{4(\beta^2 - 1)}{3\beta[(2\beta^2 - 1)\gamma - 1]}, \quad \gamma = \frac{\ln[\beta + \sqrt{\beta^2 - 1}]}{\beta\sqrt{\beta^2 - 1}}. \quad (\text{S2})$$

These expressions are consistent with those given in Tables 3.4 and 3.6 in the book by Kim and Karrila (1991). For oblate spheroids, our expressions are identical to those of Kim & Karrila, for prolate spheroids they differ by a factor of  $\beta$ , and so does Eq. (9) in the main text. As a consequence, the two formulations are equivalent for oblate and for prolate spheroids. In the main text we refer to the translational resistance coefficients in the  $\hat{\mathbf{g}}$ - and  $\hat{\mathbf{p}}$ -directions (these directions are defined in Fig. 2 in the main text). These coefficients are defined as

$$A^{(g)} \equiv \begin{cases} A_{\perp} & \text{if } \Lambda > 0 \\ A_{\parallel} & \text{if } \Lambda < 0 \end{cases}, \quad A^{(p)} \equiv \begin{cases} A_{\parallel} & \text{if } \Lambda > 0 \\ A_{\perp} & \text{if } \Lambda < 0 \end{cases}. \quad (\text{S3})$$

Recall that  $\Lambda > 0$  ( $\Lambda < 0$ ) corresponds to prolate (oblate) spheroids. The resistance tensors  $\mathbb{C}$  and  $\mathbb{H}$  in the Jeffery torque [Eq. (10) in the main text] take the form:

$$C_{ij} \equiv C_{\perp}(\delta_{ij} - n_i n_j) + C_{\parallel} n_i n_j, \quad H_{ijk} = H_0 \epsilon_{ijl} n_k n_l, \quad (\text{S4})$$

$$C_{\perp} = \frac{8a_{\parallel} a_{\perp} (\beta^4 - 1)}{9\beta^2 [(2\beta^2 - 1)\gamma - 1]}, \quad C_{\parallel} = -\frac{8a_{\parallel} a_{\perp} (\beta^2 - 1)}{9(\gamma - 1)\beta^2}, \quad H_0 = -C_{\perp} \frac{\beta^2 - 1}{\beta^2 + 1}.$$

Here  $\epsilon_{ijl}$  is the Levi-Civita tensor, and repeated indices are summed over. The particle-inertia tensor per unit mass,  $\mathbb{I}$ , has elements

$$I_{ij} = I_{\perp}(\delta_{ij} - n_i n_j) + I_{\parallel} n_i n_j, \quad \text{with } I_{\perp} = \frac{1 + \beta^2}{5} a_{\perp}^2 \quad \text{and} \quad I_{\parallel} = \frac{2}{5} a_{\perp}^2. \quad (\text{S5})$$

## II. CALCULATION OF THE TILT-ANGLE VARIANCE IN REGIMES ③, ④, AND ⑤

In this Section we describe how we determined the tilt-angle variance  $\langle \delta\varphi^2 \rangle$  in regimes ③, ④, and ⑤. Here  $\text{Sv}$  is large, and in regimes ③ and ④ the Stokes number is small. In regime ⑤, the Stokes number need not be small, but we assume that  $\delta\varphi$  remains small. In regime ③, the angular dynamics is overdamped. We discuss the overdamped angular dynamics in Sections II A and II B. Section II C describes the angular dynamics in regime ④. In Section II D we show how to approximate over- and underdamped c.o.m. dynamics, and in Section II E we summarise how to compute the tilt-angle variance in regimes ② to ④. In Section II F we discuss the tilt-angle variance in regime ⑤, where both c.o.m. and angular dynamics are underdamped.

### A. Overdamped angular dynamics: platelets

Let us assume that the matrix  $\mathbb{Y}$  [Eq. (19) in the main text] changes slowly compared to the linearized dynamics [Eq. (18a) in the main text] and that it therefore can be treated as constant at those time scales. For constant  $\mathbb{Y}$  we find that the angular dynamics, Eq. (18a), has the fixed point

$$[\delta\varphi^*, \theta^*, \omega_s^*, \omega_p^*, \omega_g^*] = \left[ \frac{\sqrt{Y_{g2}^2 + Y_{g3}^2}}{\text{sgn}(\delta\varphi)Y_{gg}}, \text{atan}\left(\frac{Y_{g3}}{Y_{g2}}\right), 0, 0, \Omega_g \right]. \quad (\text{S6})$$

The five eigenvalues of the stability matrix of the dynamics (18a) evaluated at the fixed point read

$$\lambda_{1,2} = -\frac{C_{\perp}}{2I_{\perp}\text{St}} \pm i\Omega_0, \quad \lambda_{3,4} = \lambda_{1,2}, \quad \lambda_5 = -\frac{C_{\parallel}}{I_{\parallel}\text{St}}, \quad \text{where } \Omega_0 = \frac{C_{\perp}}{2I_{\perp}\text{St}} \sqrt{4|\mathcal{A}|\text{Sv}^2 I_{\perp}\text{St} \frac{A^{(p)}}{C_{\perp}A^{(g)}} - 1}. \quad (\text{S7})$$

This shows that the fixed point is stable, so that the angular dynamics relaxes to this fixed point on the time scale  $2I_{\perp}\text{St}/C_{\perp} \sim \tau_d$  ( $I_{\parallel}\text{St}/C_{\parallel}$  is of the order  $\tau_d$  for spheroids, unless  $\beta$  is very large). In the limit of large  $\text{Sv}$ , the matrix  $\mathbb{Y}$  changes on the time scale  $\tau_s$ , Eq. (20) in the main text. We therefore expect the dynamics to follow Eq. (S6) when  $\tau_d \ll \tau_s$ . In this limit the angular dynamics is overdamped, so that only the terms inversely proportional to  $\text{St}$  matter in Eq. (18a). In addition we need to assume that  $\tau_{\varphi} \ll 1$  to ensure that  $\delta\varphi$  remains small, so that the linearisation used to derive Eq. (18a) remains valid. The assumptions above define the boundaries of regimes ② and ③ given in Section 5 of the main text.

We add a remark concerning the dynamics of  $\hat{\boldsymbol{p}}$ . To derive the expression for  $\theta^*$  in Eq. (S6), we solved  $Y_{gs} = \hat{\boldsymbol{g}}^{\text{T}}\mathbb{Y}\hat{\boldsymbol{s}} = 0$  [from the equation for  $\dot{\omega}_p$  in Eq. (18a)]. For this condition to hold,  $\theta^*$  must be chosen such that the vector  $\hat{\boldsymbol{g}}^{\text{T}}\mathbb{Y}$  is perpendicular to  $\hat{\boldsymbol{s}}$ . Since  $\hat{\boldsymbol{p}}$  is perpendicular to  $\hat{\boldsymbol{s}}$ , we find  $\theta^*$  through the relation

$$\hat{\boldsymbol{p}}(\theta^*) = \frac{\text{sgn}(\delta\varphi)}{\sqrt{Y_{g2}^2 + Y_{g3}^2}} [0, Y_{g2}, Y_{g3}], \quad (\text{S8})$$

for  $\hat{\boldsymbol{g}} = \hat{\boldsymbol{e}}_1$ . The sign is chosen so that the factor  $\text{sgn}(\delta\varphi^*)$  in Eq. (S6) equals the sign of  $\delta\varphi$  (note that  $Y_{gg}$  is positive for large settling velocities). This choice corresponds to the stable fixed point of the  $\theta$ -dynamics. We conclude that the transversal orientation  $\hat{\boldsymbol{p}}$  of platelets aligns with the vector  $[0, Y_{g2}, Y_{g3}]$ .

### B. Overdamped angular dynamics: columns

Now consider the fixed points of the angular dynamics (18b) for columns. They exist only for certain  $\mathbb{Y}$ -matrices, namely when there is a  $\theta^*$  such that  $s_i[Y_{gi}Y_{gj}/Y_{gg} - Y_{ij}]p_j|_{\theta=\theta^*} = 0$ . For large  $\text{Sv}$ , we approximate  $Y_{gi}Y_{gj}/Y_{gg} - Y_{ij} \sim O_{ij} + \Lambda S_{ij}$ . This means that fixed points of Eq. (18b) must satisfy  $\boldsymbol{s}^{\text{T}}[\mathbb{O} + \Lambda\mathbb{S}]\boldsymbol{p}|_{\theta=\theta^*} = 0$ . This equation has real solutions  $\theta^*$  if the discriminant  $\Lambda^2(S_{22} - S_{33})^2 + 4\Lambda^2 S_{23}^2 - 4O_{23}^2$  of the lower right  $2 \times 2$  block of  $\mathbb{O} + \Lambda\mathbb{S}$  is positive. Moreover, even when such fixed points exist, they have a vanishing stability exponent in the  $\theta$ -direction within the approximation considered here. Fixed points of the dynamics (18b) are therefore at best weakly stable and the dynamics does not have time to approach any fixed point within the time scale of  $\mathbb{Y}$ , as was the case for platelets.

Instead, we search for fixed points of the dynamics of  $[\delta\varphi, \omega_s, \omega_p, \omega_g]$ . Solving  $\frac{d}{dt}\delta\varphi = \frac{d}{dt}\omega_s = \frac{d}{dt}\omega_p = \frac{d}{dt}\omega_g = 0$  for general values of  $\theta$  we find:

$$[\delta\varphi^*, \omega_s^*, \omega_p^*, \omega_g^*] = \left[ \frac{Y_{gp}}{Y_{gg}}, 0, \Omega_p, \frac{Y_{gp}Y_{gs}}{Y_{gg}} - Y_{sp} \right]. \quad (\text{S9})$$

This fixed point is stable because its stability exponents have negative real parts,

$$\lambda_{1,2} = -\frac{C_{\perp}}{2I_{\perp}\text{St}} \pm i\Omega_0, \quad \lambda_3 = -\frac{C_{\perp}}{I_{\perp}\text{St}}, \quad \lambda_4 = -\frac{C_{\parallel}}{I_{\parallel}\text{St}}. \quad (\text{S10})$$

What about the  $\theta$ -dynamics? Since  $\frac{d}{dt}\theta = \omega_g \sim \omega_g^* \sim \Omega_g + \Lambda S_{sp}$  for large  $\text{Sv}$ , the variable  $\theta$  diffuses slowly in this limit. The stability time of the  $\theta$ -dynamics is  $\sim \tau_K = 1$ , so that  $\theta$  cannot follow the fixed point. In homogeneous, isotropic flows, the gradients  $\Omega_g + \Lambda S_{sp}$  are independent from  $O_{gp} + \Lambda S_{gp}$  and  $O_{gs} + \Lambda S_{gs}$ , evaluated at the same spatial position (these two combinations drive the other components of the angular velocity). Therefore we can treat  $\theta$  as an independent, uniformly distributed random variable that can be considered constant in regimes ② and ③. In summary, the  $\delta\varphi$ -dynamics of columns follows the fixed point (S9), and  $\theta$  (and thus  $\hat{\boldsymbol{p}}$ ) changes randomly albeit very slowly.

### C. Angular dynamics in regime ④

In regimes ② and ③, the flow decorrelation time due to settling,  $\tau_s$ , is larger than the time scale of the angular dynamics. Therefore the particle orientations follow the fixed points (S6) and (S9). In regime ④, by contrast,  $\tau_s$  is smaller than  $\tau_d$ . Surprisingly, we find that the variables determining the tilt-angle dynamics –  $[\delta\varphi, \theta, \omega_s, \omega_p]$  for platelets and  $[\delta\varphi, \omega_s]$  for columns – nevertheless follow the fixed points, Eqs. (S6) and (S9). This is explained by the observation that the dynamics of  $[\omega_s, \omega_p]$  (platelets) and  $\omega_s$  (columns) is fast, it fluctuates on a time scale much shorter than  $\tau_s$ . In a mean-field approximation, we can therefore replace  $\omega_s$  and  $\omega_p$  in Eq. (18) in the main text by their mean values,  $\langle\omega_p\rangle = \langle\omega_s\rangle = 0$ . The resulting mean-field equations obtained by averaging  $\dot{\omega}_s$  and  $\dot{\omega}_p$  become

$$Y_{gp} - Y_{gg}\delta\varphi = 0 \quad \text{and} \quad Y_{gs} = 0 \quad \text{for platelets,} \quad (\text{S11a})$$

$$Y_{gp} - Y_{gg}\delta\varphi = 0 \quad \text{for columns.} \quad (\text{S11b})$$

In Eq. (S11a) we neglected the terms quadratic in  $\omega$  in Eq. (18a) in the main text. Since the sign of  $\delta\varphi$  does not fluctuate, these terms have non-zero averages. However, computer simulations of the statistical model show that these terms remain bounded, even though they are proportional to  $\delta\varphi^{-1}$ . When the Stokes number is small, we therefore neglected these terms, but kept terms multiplied by  $\text{St}^{-1}$ . This results in Eqs. (S11). These equations are the same as the conditions obtained when solving Eq. (S6) for the fixed-point values of  $\delta\varphi^*$  and  $\theta^*$  (platelets), and (S9) for  $\delta\varphi^*$  (columns). We therefore conclude that the solutions for  $\delta\varphi^*$  (and  $\theta^*$  for platelets) obtained in regimes ② and ③ remain valid also in regime ④. But note that other components of  $\boldsymbol{\omega}$  cease to follow their fixed-point values in regime ④.

For all simulations shown in the figures in the main text we verified that the dynamics of  $[\omega_s, \omega_p]$  (platelets) and  $\omega_s$  (columns) is fast. For columns we can show this explicitly in regime ④ where we can replace  $W_p$  in Eq. (18) by  $-u_2$  because fluctuations of  $\boldsymbol{v}$  are much smaller than fluctuations of  $\boldsymbol{u}$  in the underdamped limit. For columns we infer that  $\delta\varphi$  satisfies the equation of a driven damped oscillator

$$\frac{d^2}{dt^2}\delta\varphi + \frac{C_\perp}{I_\perp \text{St}} \frac{d}{dt}\delta\varphi + \frac{C_\perp}{I_\perp \text{St}} |\mathcal{A}| \text{Sv}^2 \frac{A^{(p)}}{A^{(g)}} \delta\varphi = -|\mathcal{A}| \text{Sv} A^{(p)} \frac{C_\perp}{I_\perp \text{St}} u_2.$$

The solution of this equation is

$$\delta\varphi(t) = \frac{A^{(g)}\Omega_0}{\text{Sv}} \int_0^t dt_1 e^{(t_1-t)C_\perp/(2I_\perp \text{St})} \sin[\Omega_0(t_1-t)] u_2(t_1), \quad (\text{S12})$$

where  $\Omega_0 = \sqrt{|\mathcal{A}| \text{Sv}^2 C_\perp A^{(p)} / (I_\perp \text{St} A^{(g)})}$  [ $\Omega_0$  in Eq. (S7) approaches this expression in the limit of regime ④]. Taking the time derivative gives  $\omega_s(t)$ . To show that the dynamics of  $\omega_s(t)$  is faster than that of  $\delta\varphi(t)$ , we compute the correlation functions  $\langle\delta\varphi(t)\delta\varphi(t')\rangle$  and  $\langle\omega_s(t)\omega_s(t')\rangle$  using Eq. (S12). We find that  $\langle\delta\varphi(t)\delta\varphi(t')\rangle$  decays like  $C_u(t-t') = \langle u_2(t-t')u_2(0)\rangle$  and conclude that  $\delta\varphi$  decorrelates on the time scale  $\tau_s$ . To estimate the correlation time of  $\omega_s$ , we expand  $C_{\omega_s}(t-t') = \langle\omega_s(t)\omega_s(t')\rangle$  for small  $|t-t'|$ ,  $C_{\omega_s}(t-t') \sim C_{\omega_s}(0) + C''_{\omega_s}(0)t^2/2$ , and define the correlation time  $\tau_{\omega_s}$  of  $\omega_s$  in terms of the curvature of the correlation function

$$\tau_{\omega_s} = \sqrt{-C_{\omega_s}(0)/C''_{\omega_s}(0)}. \quad (\text{S13})$$

Using that  $\Omega_0 \sim \sqrt{\tau_\varphi \tau_d}$  is much larger than  $\tau_s^{-1}$  in regime ④, Eq. (S13) yields  $\tau_{\omega_s} \sim \sqrt{2}/(\Omega_0^2 \tau_s)$ . We therefore conclude for columns that the correlation time of  $\omega_s$  is much smaller than the correlation time of  $\delta\varphi$  in regime ④.

In summary, we observe that the components of  $\boldsymbol{\omega}$  fluctuate around zero with different time scales. For platelets,  $\omega_s$  and  $\omega_p$  fluctuate rapidly, the dynamics of the other components is much slower. Averaging over the fast dynamics we find that  $\delta\varphi$  and  $\theta$  follow the fixed point (S6). The conclusions for platelets are slightly different. In this case  $\omega_s$  varies rapidly. Averaging over the fast dynamics,  $\delta\varphi$  approximately follows (S9). We also observe that  $\theta$  varies slowly compared to the other variables. Taken together we conclude that  $\delta\varphi$  continues to follow its fixed point  $\delta\varphi^*$  – Eq. (S6) (platelets) and Eq. (S9) (columns) – even in regime ④, although the angular dynamics is underdamped. This means that we can use  $\delta\varphi \approx \delta\varphi^*$  in regimes ②, ③, and ④. When  $\tau_d \gg 1$ , by contrast, the dynamics is too slow to relax to these fixed points. We derive a theory for this regime in Section II F.

### D. Centre-of-mass dynamics for small tilt angle $\delta\varphi$

Since the translational degrees of freedom enter the angular dynamics (18) through  $\mathbb{Y}$  [Eq. (19) in the main text], we must determine how the slip velocity  $\boldsymbol{W}$  fluctuates. For large settling velocity we have

$$v_g \approx W_g \approx \text{Sv}/A^{(g)}, \quad Y_{gg} \approx |\mathcal{A}| \text{Sv}^2 A^{(p)}/A^{(g)}. \quad (\text{S14})$$

When particle inertia matters ( $\tau_d \gg \tau_\varphi$ ),  $\mathbf{W}$  no longer follows  $\mathbf{W}^{(0)}$ . Fluctuations of  $\mathbf{W}$  around  $\mathbf{W}^{(0)}$  affect the angular dynamics, and this means that Eq. (16) in the main text, and the corresponding result for platelets fails.

To describe the fluctuations of  $\mathbf{W}$  we use that the settling speed  $W_g$  is large. In this limit we can neglect preferential sampling due to deviations from the deterministic settling path (Gustavsson et al. 2017)  $\mathbf{x}_t^{(d)}(\hat{\mathbf{n}}_0) \equiv \mathbf{x}_0 + \text{Sv}\mathbf{W}^{(0)}(\hat{\mathbf{n}}_0)t$  when evaluating the fluid velocity at the particle position, and when evaluating its spatial gradients. Here  $\mathbf{x}_0$  is the initial particle position. Since  $\delta\varphi$  is small, we choose for the direction of  $\hat{\mathbf{n}}_0$  the stable orientation  $\varphi^*$ . The fluid velocity and its spatial gradients are therefore evaluated along the path

$$\mathbf{x}_t^{(d)} \equiv \mathbf{x}_t^{(d)}(\hat{\mathbf{n}}_0) \Big|_{\varphi_0=\varphi^*} = \mathbf{x}_0 + \frac{\text{Sv}}{A^{(g)}} \hat{\mathbf{g}} t. \quad (\text{S15})$$

If we approximate  $\mathbf{x}(t) \approx \mathbf{x}_t^{(d)}$ , then the centre-of-mass equation of motion [Eq. (7) in the main text] becomes to first order in  $\delta\varphi$

$$\dot{v}_k = \frac{A_\perp - A^{(p)}}{\text{St}} W_p p_k - \frac{A_\perp W_k}{\text{St}} + \frac{\delta\varphi \text{Sv}}{\text{St}} \left( \frac{A^{(p)}}{A^{(g)}} - 1 \right) p_k, \quad (\text{S16})$$

for  $k = 2, 3$  (transversal to  $\hat{\mathbf{g}}$ ), and  $\mathbf{W} = \mathbf{v} - \mathbf{u}(\mathbf{x}_t^{(d)}, t)$ .

### E. Tilt-angle variance in regimes ②, ③, and ④

We start with platelets. To obtain the corresponding dynamics of  $Y_{gk}$ , we differentiate Eq. (19) in the main text w.r.t. time using Eq. (S16) and set  $\delta\varphi \approx \delta\varphi^*$  and  $\theta \approx \theta^*$  [Eq. (S6)]. This yields:

$$\dot{Y}_{gk} = -\frac{A^{(g)}}{\text{St}} Y_{gk} - |\mathcal{A}| A^{(p)} \text{Sv} \dot{v}_k - \dot{O}_{1k} - |\Lambda| \dot{S}_{1k} - \frac{A^{(p)}}{\text{St}} (O_{1k} + |\Lambda| S_{1k}) \quad (\text{S17})$$

for  $k = 2, 3$ . Integrating this differential equation we find:

$$Y_{gk}(t) = -A^{(p)} |\mathcal{A}| \text{Sv} u_k(t) - O_{1k}(t) - |\Lambda| S_{1k}(t) + \frac{A^{(g)}}{\text{St}} \int_0^t dt_1 e^{(t_1-t)A^{(g)}/\text{St}} \left[ A^{(p)} |\mathcal{A}| \text{Sv} u_k(t_1) + \left( 1 - \frac{A^{(p)}}{A^{(g)}} \right) (O_{1k}(t_1) + |\Lambda| S_{1k}(t_1)) \right]. \quad (\text{S18})$$

Here and in the following we use the notation  $\mathbf{u}(t) \equiv \mathbf{u}(\mathbf{x}_t^{(d)}, t)$ , also for the fluid-velocity gradients. Inserting Eqs. (S18) and (S14) into Eq. (S6) we obtain an expression for  $\delta\varphi^*$ . We find the tilt-angle variance by squaring and averaging  $\delta\varphi^*$ . Assuming homogeneous and isotropic fluid-velocity statistics yields:

$$\langle \delta\varphi^2 \rangle = f_\Lambda \left\{ \frac{A^{(g)2}}{\text{Sv}^2} C_u(0) + \frac{A^{(g)2}}{A^{(p)2} |\mathcal{A}|^2 \text{Sv}^4} C_B(0) + \frac{A^{(g)}}{|\mathcal{A}|^2 \text{St} \text{Sv}^4} \int_0^\infty dt e^{-A^{(g)t/\text{St}}} \left[ \left( 1 - \frac{A^{(g)}}{A^{(p)2}} \right) C_B(t) + 2A^{(g)} |\mathcal{A}| \text{Sv} C_X(t) - A^{(g)2} |\mathcal{A}|^2 \text{Sv}^2 C_u(t) \right] \right\}, \quad (\text{S19})$$

where we set  $f_\Lambda = 2$  for  $\Lambda < 0$  (platelets). This is our main result, Eq. (23) in the main text, for the tilt-angle variance of platelets settling in a turbulent flow, expressed in terms of the correlation functions of fluid velocities and fluid-velocity gradients,  $C_B(t) = \langle O_{12}(t) O_{12}(0) + 2|\Lambda| O_{12}(t) S_{12}(0) + \Lambda^2 S_{12}(t) S_{12}(0) \rangle$ ,  $C_u(t) = \langle u_2(t) u_2(0) \rangle$  and  $C_X(t) = \langle u_2(t) [O_{12}(0) + |\Lambda| S_{12}] \rangle$  (Section III).

For columns the variance of  $\delta\varphi$  is obtained by averaging  $[\delta\varphi^*]^2$  in Eq. (S9) over independent, uniformly distributed values of  $\theta$ , resulting in

$$\langle [\delta\varphi^*]^2 \rangle_\theta = \frac{Y_{g2}^2 + Y_{g3}^2}{2Y_{gg}^2}. \quad (\text{S20})$$

We were surprised to find that this result for columns equals  $\frac{1}{2}[\delta\varphi^*]^2$  for platelets, Eq. (S6). In general the dynamics of  $Y_{gk}$  for columns is different from Eq. (S18). However, the combination  $Y_{g2}^2 + Y_{g3}^2$  is the same for the two kinds of particles within our approximations, and in both cases  $Y_{gg}$  is given by Eq. (S14). This means that  $\langle \delta\varphi^2 \rangle$  takes the form of Eq. (S19) divided by two. We take this factor into account by defining  $f_\Lambda = 1$  for  $\Lambda > 0$  (columns).

### F. Tilt-angle variance in regime ⑤

In this regime both the c.o.m. and the angular dynamics are underdamped. The settling velocity is large, and the Jeffery torque [Eq. (10) in the main text] does not matter. Therefore we can simplify Eq. (18) in the main text by setting  $W_g = Sv/A^{(g)}$ ,  $W_k = -u_k$ , and  $\mathbb{A} = 0$ . We can assume that  $\theta$  is an independent variable, allowing us to replace  $u_p$  by  $u_2$  and  $u_s$  by  $u_3$ . When  $\tau_s$  is the smallest time scale, we may approximate the  $\delta\varphi$ -dynamics as Langevin equations on the form  $\delta\mathbf{X} = \mathbf{V}\delta t + \delta\mathbf{F}$ . For columns, the relevant variables are  $\mathbf{X} = [\delta\varphi, \omega_s]$ , the drift velocity  $\mathbf{V}$  is given by

$$\mathbf{V} = \left[ \omega_s, -\frac{C_\perp}{I_\perp \text{St}} \left( \omega_s + \frac{A^{(p)}}{A^{(g)}} |\mathcal{A}| \text{Sv}^2 \delta\varphi \right) \right], \quad (\text{S21})$$

and the stochastic driving takes the form  $\delta\mathbf{F} = [0, \delta f]$ . Here  $\delta f$  is Gaussian white noise with vanishing mean and variance  $\langle \delta f^2 \rangle = 2D\delta t$ , where  $D$  is determined by the integral of the fluid-velocity correlations:

$$D = \frac{C_\perp}{I_\perp \text{St}} |\mathcal{A}|^2 A^{(p)2} \text{Sv}^2 \frac{1}{2} \int_{-\infty}^{\infty} dt C_u(t). \quad (\text{S22})$$

For platelets we must take  $\mathbf{X} = [\delta\varphi, \omega_s, \omega_p]$ ,

$$\mathbf{V} = \left[ \omega_s, -\frac{C_\perp}{I_\perp \text{St}} \left( \omega_s + \frac{A^{(p)}}{A^{(g)}} |\mathcal{A}| \text{Sv}^2 \delta\varphi \right) + \frac{\omega_p^2}{\delta\varphi}, -\frac{C_\perp}{I_\perp \text{St}} \omega_p - \frac{\omega_p \omega_s}{\delta\varphi} \right], \quad (\text{S23})$$

and  $\delta\mathbf{F} = [0, \delta f_2, \delta f_3]$  with  $\langle \delta f_i \delta f_j \rangle = 2\delta_{ij} D \delta t$ . From the corresponding Fokker-Planck equations we obtain recursions for the moments of components of  $\mathbf{X}$  that can be solved for the moments of  $\delta\varphi$ . For columns we find that  $\delta\varphi$  is Gaussian distributed with variance

$$\langle \delta\varphi^2 \rangle = |\mathcal{A}| A^{(g)} A^{(p)} \frac{1}{2} \int_{-\infty}^{\infty} dt C_u(t). \quad (\text{S24})$$

In the statistical model the integral evaluates to  $\sqrt{2\pi} \ell^3 A^{(g)} / (30 \text{Sv})$ . It follows that the tilt-angle variance is proportional to  $\text{Sv}^{-1}$  in regime ⑤, see Eq. (25) in the main text. For platelets we infer that  $\delta\varphi^2$  is exponentially distributed with mean equal to twice the variance of rods. Note that this factor of 2 (or  $f_\Lambda$ ) emerged also in regimes ② to ④. In regime ⑤ this factor is a consequence of the fact that the distributions of  $\delta\varphi$  have the same parameter for columns and platelets.

In summary, particle inertia results in a slow decay of the tilt-angle variance at large Stokes numbers (regime ⑤),  $\langle \delta\varphi^2 \rangle \propto \text{Sv}^{-1}$ . The same caveat as for regime ④ applies: the settling time  $\tau_s$  must be larger than the viscous time  $a^2/\nu$ , a necessary condition for the steady approximation for the inertial torque to hold.

### III. ANALYTICAL EVALUATION OF THE TILT-ANGLE VARIANCE IN THE STATISTICAL MODEL

In the statistical model (Gustavsson and Mehlig 2016) the fluid-velocity field is generated from a vector potential,  $\mathbf{u}(\mathbf{x}, t) = \nabla \wedge \Psi / \sqrt{6}$ , where the components  $\Psi_j(\mathbf{x}, t)$  of  $\Psi$  are Gaussian random functions with vanishing mean and correlation functions (in units made dimensionless using the Kolmogorov scales)

$$\langle \Psi_i(\mathbf{x}, t) \Psi_j(\mathbf{x}', t') \rangle = \delta_{ij} \frac{\ell^4}{5} \exp \left[ -\frac{|\mathbf{x} - \mathbf{x}'|^2}{2\ell^2} - \frac{|t - t'|}{\sqrt{5}\text{Ku}} \right]. \quad (\text{S25})$$

Differentiating this correlation function w.r.t. the spatial coordinate and evaluating the spatial coordinate along deterministic settling trajectories (S15) gives the following correlation functions needed to evaluate Eq. (S19)

$$C_B(t) = \frac{5 + 3\Lambda^2}{60} C_0(t) \left[ 1 - \frac{(1 + |\Lambda|)(9 + 5|\Lambda|)}{2(5 + 3\Lambda^2)} \frac{t^2}{\tau_s^2} + \frac{(1 + |\Lambda|)^2}{2(5 + 3\Lambda^2)} \frac{t^4}{\tau_s^4} \right], \quad (\text{S26a})$$

$$C_u(t) = \frac{\ell^2}{15} C_0(t) \left[ 1 - \frac{t^2}{2\tau_s^2} \right], \quad (\text{S26b})$$

$$C_X(t) = \frac{\ell}{60} (5 - 3|\Lambda|) C_0(t) \frac{t}{\tau_s} \left[ 1 - \frac{1 - |\Lambda|}{5 - 3|\Lambda|} \frac{t^2}{\tau_s^2} \right], \quad (\text{S26c})$$

$$\text{with } C_0(t) = e^{-t^2/(2\tau_s^2) - |t|/(\sqrt{5}\text{Ku})}. \quad (\text{S26d})$$

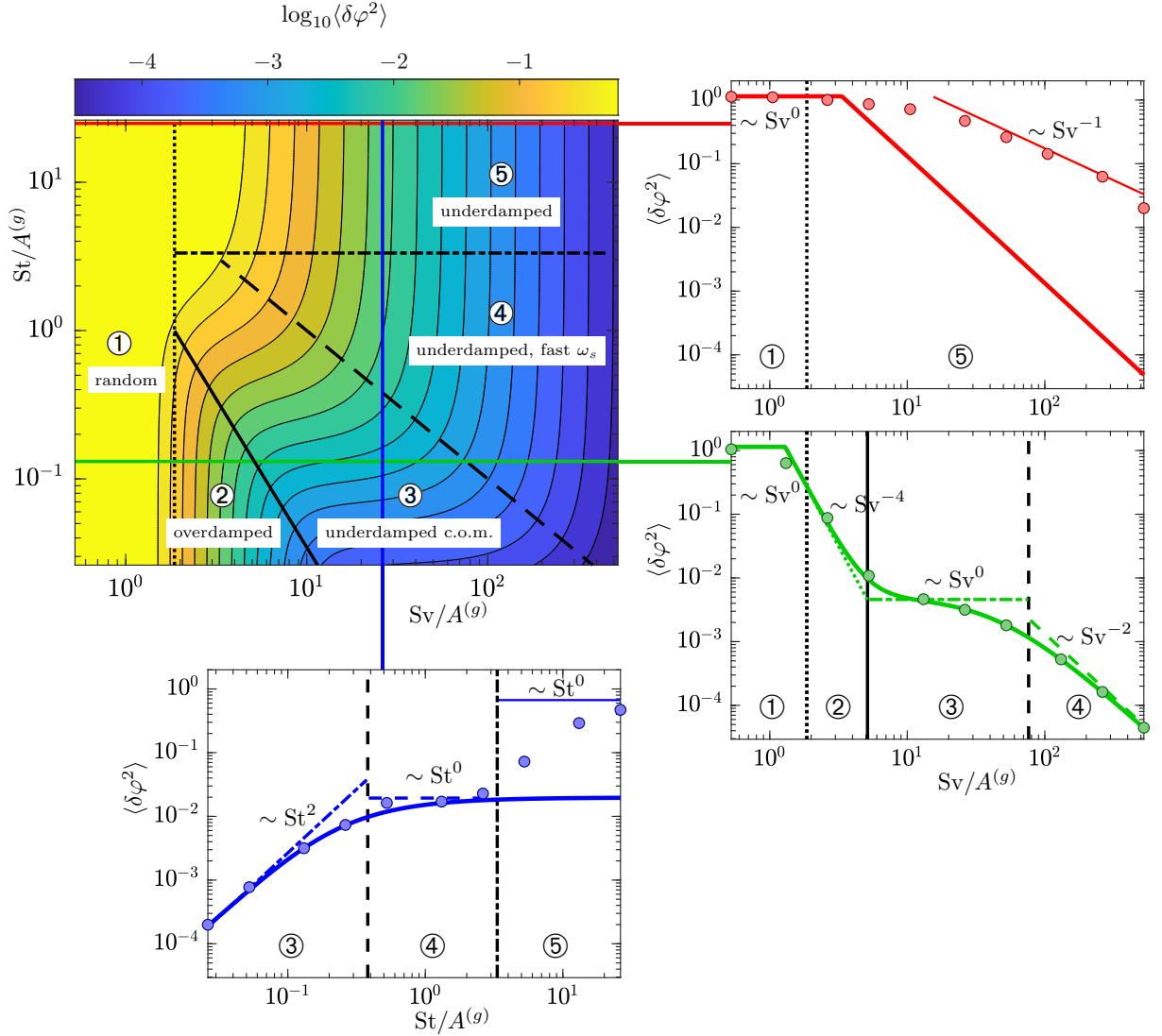


FIG. S1: —Phase diagram of asymptotic regimes for the tilt-angle variance  $\langle \delta\varphi^2 \rangle$  for regimes ②–④ based on Eq. (S27), evaluated with  $C_0(t)$  at finite  $Ku$ , Eq. (S26d). The variance  $\langle \delta\varphi^2 \rangle$  is cut off at the value  $\pi - 2$  for uniformly distributed angles. Parameters and axis ranges are identical to Fig. 3 in the main text (see text). Subpanels show  $\langle \delta\varphi^2 \rangle$  evaluated along slices with constant  $St/A^{(g)}$  (horizontal solid lines in the phase diagram) or constant  $Sv/A^{(g)}$  (vertical solid line). The subpanels show data taken from Fig. 3 in the main text (markers), Eq. (S27) (thick solid lines), and the asymptotes (24a) (dotted line), (24b) (dash-dotted lines), (24c) (dashed lines), and (25) (thin solid lines) from the main text.

Inserting these correlation functions into Eq. (S19) yields upon integration

$$\begin{aligned}
\langle \delta\varphi^2 \rangle = & \frac{f_\Lambda}{30} \left[ \frac{2A^{(g)2}St^2(5 + 3\Lambda^2) + \tau_s^2 A^{(g)2}(A^{(p)2} - A^{(g)2})(1 - |\Lambda|)^2 + 4(A^{(p)2} - A^{(g)2})St^2(1 + |\Lambda|)^2}{4A^{(p)2} \mathcal{A}^2 St^2 Sv^4} \right. \\
& + \tau_s^2 - \tau_s^2 \frac{A^{(g)}(1 - |\Lambda|)}{|\mathcal{A}| St Sv^2} + \left( (A^{(g)2} - A^{(p)2}) \frac{\tau_s^4 A^{(g)4} (1 - |\Lambda|)^2 + \tau_s^2 A^{(g)2} St^2 (\Lambda^2 + 2|\Lambda| - 3) + 4St^4 (1 + |\Lambda|)^2}{4\tau_s^2 A^{(g)2} A^{(p)2} \mathcal{A}^2 St^2 Sv^4} \right), \quad (S27) \\
& \left. + \frac{\tau_s^2 A^{(g)2} (1 - |\Lambda|) - 2St^2}{A^{(g)} |\mathcal{A}| St Sv^2} + \frac{St^2}{A^{(g)2}} - \tau_s^2 \right) \mathcal{H} \left( \frac{\tau_s A^{(g)}}{\sqrt{2} St} \right) \Big]
\end{aligned}$$

where  $\mathcal{H}(x) = 2x^2[1 - \sqrt{\pi}xe^{x^2}\text{erfc}(x)]$ . The result (S27) is valid for both platelets and columns in regimes ② to ④. It is written here using the limit  $Ku \rightarrow \infty$ , i.e.  $C_0(t) = e^{-t^2/(2\tau_s^2)}$ . Fig. S1 shows the theory (S27) against  $Sv/A^{(g)}$  and  $St/A^{(g)}$  with  $\beta = 0.1$ ,  $\ell = 10$ , and  $Ku = 10$ . The theory is cut off at the tilt-angle variance of uniformly distributed

angles, obtained by averaging  $\delta\varphi^2$  over the distribution,  $\rho(\delta\varphi) = |\sin \delta\varphi|/2$  for  $-\pi/2 \leq \delta\varphi < \phi/2$ .

Comparing the analytical results plotted in Fig. S1 to the statistical-model simulations in Fig. 3 (main text) shows excellent agreement in regimes ② to ④ where the theory applies. As expected, Eq. (S27) fails in the limit of large St. The upper inset in Figure S1 shows that the simulation results approach the asymptote (25), derived from Eq. (S24) above, in the limit of large St and Sv (regime ⑤). The other insets confirm that the simulation results asymptotically approach the power-laws, Eqs. (24).

#### IV. EMPIRICAL PARAMETERS

Bréon and Dubrulle (2004) considered alignment of hexagonal platelets of thickness  $h$ , with diameters  $d = 2a$  in the range 0.1 to 3 mm, and aspect ratios  $h/d \sim 2d^{-0.55}$  with  $h$  and  $d$  in  $\mu\text{m}$ . In other words, the aspect ratio varied from  $\beta = 0.16$  for  $d = 100 \mu\text{m}$  to  $\beta = 0.024$  for  $d = 3 \text{ mm}$ . For these aspect ratios the shape coefficient  $A^{(g)}$  is very close to the asymptotic value at  $\beta \rightarrow \infty$ :  $A^{(g)} \approx 0.85$ . Typical turbulent dissipation rates in clouds range from  $\mathcal{E} \sim 1$  to  $1000 \text{ cm}^2/\text{s}^3$  (Grabowski and Vaillancourt 1999). The mass density of air is  $\rho_f \sim 1.2 \text{ kg}/\text{m}^3$ , with kinematic viscosity  $\nu \sim 10^{-5} \text{ m}^2/\text{s}$ . For a particle-mass density of  $\rho_p = 0.9 \times 10^{-3} \text{ g}/\text{cm}^3$ , values of St, Sv,  $\text{Re}_p$  are given in Table S1, for  $a = d/2 = 50, 150, 300 \mu\text{m}$ , and for two values of  $\mathcal{E}$  ( $\mathcal{E} = 10 \text{ cm}^2/\text{s}^3$  and  $\mathcal{E} = 1000 \text{ cm}^2/\text{s}^3$ ).

Jucha et al. (2018) and Sheikh et al. (2020) analysed collisions of ice crystals settling in turbulence using model equations of motion in combination with DNS of turbulence, for  $\mathcal{E} \approx 1, 16$ , and  $246 \text{ cm}^2/\text{s}^3$ .

Kramel (2017) measured angular dynamics of triads settling in a turbulent water tank (fluid mass density  $\rho_f = 0.995 \text{ g}/\text{cm}^3$ , viscosity  $\nu = 0.96 \times 10^{-6} \text{ m}^2/\text{s}$ ). The turbulent dissipation rate  $\mathcal{E}$  ranged from 0.04 to  $60 \text{ mm}^2/\text{s}^3$ . The corresponding Kolmogorov time  $\tau_K$  ranges from 5 s to 0.13 s, and the Kolmogorov length  $\eta_K$  from  $2.16 \times 10^{-3} \text{ m}$  to  $3.3 \times 10^{-4} \text{ m}$ . The small triads fabricated by Kramel were made out of slender fibres of radius  $225 \mu\text{m}$  and length 4.5 mm. A triad turns like a disk with radius 4.5 mm and aspect ratio 1/20, but with a different resistance coefficient  $A^{(g)}$  because the particle is ramified. We estimated the resistance coefficient  $A^{(g)}$  from the experimentally observed settling speed in quiescent fluid using (in dimensional units)  $W = g\tau_p/A^{(g)}$ . The particles were only slightly heavier than the fluid, so we used (in dimensional units)

$$\tau_p = \frac{2}{9} \left( \frac{\rho_p}{\rho_f} - 1 \right) \frac{a_{\parallel} a_{\perp}}{\nu} \quad (\text{S28})$$

instead of Eq. (6) in the main text to estimate the particle response time. With  $W = 23.2 \text{ mm}/\text{s}$  (Kramel 2017) we found  $A^{(g)} \approx 15.4$ . We note that the other shape coefficients too are quite different for a ramified particle compared with a solid platelet (Section I). The particle Reynolds number is too large for the model to apply quantitatively, and we also note that the particles were larger than  $\eta_K$ .

Esteban et al. (2020) studied the settling of small aluminium disks in a turbulent water tank ( $\rho_f = 0.996 \text{ g}/\text{cm}^3$ ,  $\nu = 1.02 \times 10^{-6} \text{ m}^2/\text{s}$ ). Turbulent dissipation rate (Esteban et al. 2019)  $\mathcal{E} = 1.4 \times 10^{-3} \text{ m}^2/\text{s}^3$ ; Kolmogorov scales  $\tau_K = 0.026 \text{ s}$ ,  $\eta_K = 0.16 \text{ mm}$ ,  $u_K = 6.2 \text{ mm}/\text{s}$ ; Reynolds number  $\text{Re}_{\lambda} = 50$ . The disks have diameter  $d = 10 \text{ mm}$ , height  $h = 0.5 \text{ mm}$ , as well as  $d = 15 \text{ mm}$ ,  $h = 1 \text{ mm}$ . The particle-mass density is  $\rho_p = 2.7 \text{ g}/\text{cm}^3$ . Particle Reynolds numbers estimated from the Stokes settling velocity are very large, this shows that the small- $\text{Re}_p$  approximation we used up to this point must break down. Instead we based our estimate in Table S1 upon the measured average settling speed. For the smaller disk,  $\langle W \rangle = 9.5 \text{ cm}/\text{s}$ , and for the larger disk  $\langle W \rangle = 15.8 \text{ cm}/\text{s}$ . Using this we estimate  $\text{Sv}/A^{(g)} \sim \langle W \rangle \tau_K / \eta_K = 15.4$  and 25.7. The corresponding particle Reynolds numbers are 95 and 158, and  $\text{St}/A^{(g)} \sim \text{Fr Sv}/A^{(g)} = 0.36$  and 0.6. While  $\text{St}/A^{(g)}$  and  $\text{Sv}/A^{(g)}$  are appropriate measures of particle inertia and settling speed near the viscous limit, the regime we considered in this article, at large particle Reynolds numbers it is more appropriate to use the inertia parameter  $I^* \propto \rho_p I_{\perp} / (\rho_f a^2)$ , and the Archimedes number  $\text{Ar} = \sqrt{\frac{3}{16} (\rho_p / \rho_f - 1) g a_{\parallel}}$  (Auguste et al. 2013; Esteban et al. 2020; Willmarth et al. 1964).

TABLE S1: Values of dimensionless parameters

Reference	$a$ [ $\mu\text{m}$ ]	$\beta$	$\rho_p$ [ $\text{g}/\text{cm}^3$ ]	$\varrho_f$ [ $\text{g}/\text{cm}^3$ ]	$\nu$ [ $\text{cm}^2/\text{s}$ ]	$\mathcal{E}$ [ $\text{cm}^2/\text{s}^3$ ]	Fr	$St/A^{(g)}$	$Sv/A^{(g)}$	$A^{(g)}$	$Re_p$
Bréon and Dubrulle (2004) (hexagonal platelets)	50	$\frac{1}{6}$	0.9	$1.2 \times 10^{-3}$	0.1	10	0.01	0.08	7.9	0.86	0.4
	150	$\frac{1}{12}$	0.9	$1.2 \times 10^{-3}$	0.1	10	0.01	0.37	36	0.85	5.4
	300	$\frac{1}{16}$	0.9	$1.2 \times 10^{-3}$	0.1	10	0.01	1.1	107	0.85	32
	50	$\frac{1}{6}$	0.9	$1.2 \times 10^{-3}$	0.1	1000	0.32	0.81	2.5	0.86	0.4
	150	$\frac{1}{12}$	0.9	$1.2 \times 10^{-3}$	0.1	1000	0.32	3.7	11.4	0.85	5.4
	300	$\frac{1}{16}$	0.9	$1.2 \times 10^{-3}$	0.1	1000	0.32	11	34	0.85	32
Jucha et al. (2018) & Sheikh et al. (2020) (disks)	150	0.01	0.92	$1.4 \times 10^{-3}$	0.11	1	0.0018	0.01	5.9	0.85	0.46
	150	0.02	0.92	$1.4 \times 10^{-3}$	0.11	1	0.0018	0.02	11.8	0.85	0.93
	150	0.01	0.92	$1.4 \times 10^{-3}$	0.11	16	0.014	0.04	3	0.85	0.46
	150	0.02	0.92	$1.4 \times 10^{-3}$	0.11	16	0.014	0.08	5.9	0.85	0.93
	150	0.05	0.92	$1.4 \times 10^{-3}$	0.11	16	0.014	0.2	14.8	0.85	2.3
	150	0.01	0.92	$1.4 \times 10^{-3}$	0.11	246	0.11	0.16	1.5	0.85	0.46
Kramel (2017) (small triads)	$4.5 \times 10^3$	$\frac{1}{20}$	1.14	0.995	$9.6 \times 10^{-3}$	$0.4 \times 10^{-3}$	$9 \times 10^{-3}$	$0.5 \times 10^{-6}$	$52$	14.44	109
	$4.5 \times 10^3$	$\frac{1}{20}$	1.14	0.995	$9.6 \times 10^{-3}$	$7.5 \times 10^{-3}$	$83 \times 10^{-6}$	$2 \times 10^{-3}$	25	14.44	109
	$4.5 \times 10^3$	$\frac{1}{20}$	1.14	0.995	$9.6 \times 10^{-3}$	$9.5 \times 10^{-2}$	$0.56 \times 10^{-2}$	$7 \times 10^{-3}$	13	14.44	109
	$4.5 \times 10^3$	$\frac{1}{20}$	1.14	0.995	$9.6 \times 10^{-3}$	0.3	$1.3 \times 10^{-3}$	$13 \times 10^{-3}$	10	14.44	109
	$4.5 \times 10^3$	$\frac{1}{20}$	1.14	0.995	$9.6 \times 10^{-3}$	0.5	$1.9 \times 10^{-3}$	$17 \times 10^{-3}$	8.8	14.44	109
	$4.5 \times 10^3$	$\frac{1}{20}$	1.14	0.995	$9.6 \times 10^{-3}$	0.6	$2.2 \times 10^{-3}$	$18.7 \times 10^{-3}$	8.4	14.44	109
Esteban et al. (2020) (disks)	$5 \times 10^3$	$\frac{1}{20}$	2.7	0.996	0.01	14	0.023	0.36	15.4	0.85	95
	$7.5 \times 10^3$	$\frac{1}{15}$	2.7	0.996	0.01	14	0.023	0.6	25.7	0.85	158

- 
- Auguste, F., J. Magnaudet, and D. Fabre, 2013: Falling styles of disks. *Journal of Fluid Mechanics*, **719**, 388–405.
- Bréon, F.-M., and B. Dubrulle, 2004: Horizontally oriented plates in clouds. *Journal of the Atmospheric Sciences*, **61**, 2888–2898.
- Esteban, L. B., J. S. Shrimpton, and B. Ganapathisubramani, 2019: Laboratory experiments on the temporal decay of homogeneous anisotropic turbulence. *Journal of Fluid Mechanics*, **862**, 99–127.
- Esteban, L. B., J. S. Shrimpton, and B. Ganapathisubramani, 2020: Disks settling in turbulence. *Journal of Fluid Mechanics*, **883**, A58.
- Grabowski, W. W., and P. Vaillancourt, 1999: Comments on ‘Preferential Concentration of Cloud Droplets by Turbulence: Effects on the Early Evolution of Cumulus Cloud Droplet Spectra’. *Journal of the Atmospheric Sciences*, **56** (10), 1433–1436.
- Gustavsson, K., J. Jucha, A. Naso, E. Lévêque, A. Pumir, and B. Mehlig, 2017: Statistical model for the orientation of nonspherical particles settling in turbulence. *Phys. Rev. Lett.*, **119**, 254501.
- Gustavsson, K., and B. Mehlig, 2016: Statistical models for spatial patterns of heavy particles in turbulence. *Adv. Phys.*, **65**, 1.
- Jucha, J., A. Naso, E. Lévêque, and A. Pumir, 2018: Settling and collision between small ice crystals in turbulent flows. *Phys. Rev. Fluids*, **3**, 014604.
- Kim, S., and S. J. Karrila, 1991: *Microhydrodynamics: principles and selected applications*. Butterworth-Heinemann, Boston.
- Kramel, S., 2017: Non-spherical particle dynamics in turbulence. Ph.D. thesis, Wesleyan University.
- Sheikh, M. Z., K. Gustavsson, D. Lopez, E. Leveque, B. Mehlig, A. Pumir, and A. Naso, 2020: Collision between small ice crystals in turbulent flows: effect of fluid inertia.
- Willmarth, W. W., N. E. Hawk, and R. L. Harvey, 1964: Steady and unsteady motions and waks of freely falling disks. *Phys. Fluids*, **7**, 197–208.